8-8-2022

Density functional theory study of oxygen vacancy formation and doping on wollastonite surfaces

Vedgopal Balasubramanian Govindhram
vg8433@rit.edu

Density functional theory study of oxygen vacancy formation and doping on wollastonite surfaces

Vedgopal Balasubramanian Govindhram

A thesis submitted in partial fulfillment of the
requirements for the degree of:
Master of Science in Materials Science and Engineering

Supervised by

Dr. Pratik Dholabhai

School of Chemistry and Materials Science

College of Science

August 8, 2022

Rochester Institute of Technology, Rochester 14623

Committee Approval

Thesis Advisor

Dr. Pratik Dholabhai Date

Assistant Professor, School of Physics and Astronomy, College of Science Program

Faculty, School of Chemistry and Materials Science

Committee Members

Dr. Bruce E. Kahn Date

Adjunct Professor, School of Chemistry and Materials Science

Dr. Ke Xu Date

Assistant Professor, School of Physics and Astronomy, College of Science

Program Faculty, School of Chemistry and Materials Science

Program Faculty, Microsystems Engineering

Dr. Emiliano Brini Date

Assistant Professor, School of Chemistry and Materials Science

Acknowledgements

This work is supported by the Alfred P. Sloan Foundation Grant Number 2021-14167. This work used computational resources provided by the Extreme Science and Engineering Discovery Environment (XSEDE), which is supported by the National Science Foundation (NSF) grant number ACI-1548562. I would like to thank the Rochester Institute of Technology for partial computing resources from Research Computing.

I would also like to thank my advisor Dr. Pratik Dholabhai for his teaching, guidance, and support throughout the past year. I thank him for major contributions to both my work and I as a person. Next, I would like to thank my committee members: Dr. Bruce E. Kahn, Dr. Ke Xu, and Dr. Emiliano Brini for their support and guidance inside and outside the classroom. I am very grateful to Brian Luan for his continued help throughout my thesis work. I thank my family and friends for their undying love and support. Lastly, I would also like to thank the students and faculty at the Rochester Institute of Technology, specifically those in the College of Science and the School of Chemistry and Materials Science.

Abstract

In recent times, the rising amount of carbon dioxide (CO_2) in the atmosphere have caused a concerning increase in global warming. To combat global warming, several negative emissions technologies have been employed. One such technology is Enhanced Rock Weathering (ERW), wherein CO_2 is trapped as thermodynamically stable carbonates in silicate minerals that are exposed to the atmosphere. This process happens via mineral carbonation. Wollastonite ($CaSiO_3$) is one such silicate that has applications in ERW. Our study is focused on utilizing density functional theory-based calculations to investigate the thermodynamic stability of oxygen vacancies on the surfaces of wollastonite mineral. Formation of oxygen vacancy naturally requires large amounts of energy. Oxygen vacancy formation is more favorable on the surface rather than in the bulk of the wollastonite mineral. We further studied if adding dopants (aluminum dopants) on the surface of the mineral is thermodynamically favorable and evaluated their overall impact on oxygen vacancy formation. Formation of oxygen vacancies on the wollastonite surfaces is found to be an endothermic process, whereas addition of aluminum dopants makes it an exothermic process. This fundamental knowledge will be instrumental in enhancing the reactivity of wollastonite minerals for effective sequestration of carbon dioxide using ERW.

Table of Contents

List of Figures and Tables

Table of Abbreviations

Abbreviation	Meaning
DFT	Density Functional Theory
KS	Kohn Sham
CO_2	Carbon dioxide
DAC	Direct Air Capture
ERW	Enhanced Rock Weathering
Å	Angstroms
PAW	Projector Augmented-Wave
XC	Exchange-correlation

Chapter 1 – Introduction

In recent times, there have been numerous advancements in technologies and innovations. But most of them come at the cost of environmental risks. Among those risks which has been a cause for high concern is global warming. Global warming is the long-term warming of the earth's overall temperature[1]. It is caused by the heat trapping air pollutants that collect in the atmosphere, which absorb sunlight and solar radiation that have bounced off the earth's surface. These heat trapping pollutants known as greenhouse gases are mainly carbon dioxide, methane, nitrous oxide, water vapor and synthetic fluorinated gases. Their impact is called the greenhouse effect. Among these greenhouse gases, carbon dioxide is present in vast amounts in the atmosphere leading to global warming. Carbon dioxide produced from human activities is primarily due to the burning of fossil fuels such as coal, oil, gasoline, and natural gas[2].

To combat the rising amounts of carbon dioxide in the atmosphere, scientists and researchers all around the world are trying different ways to sequester carbon dioxide. Carbon sequestration secures carbon dioxide to prevent it from entering the earth's atmosphere[2]. The idea is to stabilize carbon in solid and dissolved forms. The three main types of carbon sequestration are biological, geological and technological carbon sequestration[3].

Biological carbon sequestration is the storage of carbon dioxide in vegetation such as grasslands or forests, as well as in soils and oceans. Geological carbon sequestration is the process of storing carbon dioxide in underground geologic formations, or rocks. Typically, carbon dioxide is captured from an industrial source and injected into porous rocks for long term storage. Technological

carbon sequestration is the removal and storage of carbon dioxide from the atmosphere using innovative technologies such as Direct Air Capture (DAC) and using engineered molecules capable of changing shapes. Apart from these, researchers are also starting to look beyond removal of carbon dioxide and are now looking at more ways it can be used as resource as in graphene production.

Our primary focus in this thesis is of one of the geological carbon sequestration methods called as Enhanced Rock Weathering (ERW)[4]. This is a dominant form of chemical weathering, a naturally occurring process. The carbon dioxide emitted from the volcanic activities rises into the atmosphere and undergo two types of rock weathering: *Carbonate rock weathering* and *silicate rock weathering.* The reactions occurring during carbonate rock weathering and silicate rock weathering are shown below:

$$CO_2 + H_2O + CaCO_3 \rightarrow Ca^{2+} + 2\,HCO_3^- \quad (1.1)$$

$$2CO_2 + H_2O + CaSiO_3 \rightarrow Ca^{2+} + 2\,HCO_3^- + SiO_2 \quad (1.2)$$

In carbonate rock weathering, the carbon dioxide reacts with the carbonate rocks ($CaCO_3$) in the presence of water vapor in the atmosphere to form calcium ions and bicarbonate ions. About 95% of the earth's crust and mantle is made of silicate minerals and hence, silicate rock weathering is more common than carbonate rock weathering and will be our primary focus. In silicate rock weathering, the carbon dioxide reacts with the silicate rocks ($CaSiO_3$) in the presence of water vapor in the atmosphere to form calcium ions, bicarbonate ions and silicon dioxide. The calcium ions and bicarbonate ions are transported to the oceans by rivers where they undergo carbonate precipitation to form calcium carbonate ($CaCO_3$) which deposits at the bottom of the ocean floor and are buried, thus no longer warming the climate. The calcium carbonate undergoes metamorphism where it reacts with silicon dioxide (SiO_2) to form $CaSiO_3$ and CO_2. The CO_2 is then released into the atmosphere by

volcanic activities thus starting the weathering process all over again[4]. This entire rock weathering process is a cycle, and it takes thousands of years for the atmospheric CO_2 to be consumed. Because of the slow occurring nature of this rock weathering process, scientists and researchers have been developing novel silicates that allow for faster weathering. Wollastonite is one such that is of primary interest and will be our main focus.

Wollastonite ($CaSiO_3$) is a naturally occurring calcium silicate that can be considered fast reacting compared to other naturally occurring silicates. Wollastonite naturally occurs in three forms - triclinic wollastonite, monoclinic (or para-) wollastonite, and pseudo- or (cyclo-) wollastonite with triclinic being the most common. Triclinic wollastonite contains chains of silicon-oxygen tetrahedrons coordinated by calcium ions. Industrial mining of wollastonite is performed for its usage in the ceramic and metallurgic sectors; wollastonite can also be synthesized in the lab from the mixing limestone and silicon dioxide with sintering. Calcium silicates are preferred over their magnesium counterparts because of increased reactivity and less environmental side effects of the calcium cation.

The primary goal of this thesis is to elucidate the thermodynamic formation of oxygen vacancies on wollastonite surfaces and investigate if doping the surface of wollastonite can further aid in the formation of oxygen vacancies. The basic idea is to use the result of these studies to enhance the surface reactivity of wollastonite which in turn can help in efficient carbon sequestration on the wollastonite surfaces.

Chapter 2 – Theoretical Background

2.1 Density Functional Theory

Density Functional Theory (DFT) is a widespread computational method to model ground state electronic structures and properties that arise from it[5]. The goal of many quantum mechanical computations is to approximate wavefunction solutions to the Schrödinger equation for the physical system under study. Conversely, DFT describes a system in terms of its electron density instead of it's many-body wavefunction. Thomas[6], Fermi[7] and Dirac[8] envisioned that a system of electrons could be modeled from their uniform electron gas densities. Thomas-Fermi theory formed the basis of DFT but was not able to predict bonding. The first principles of DFT were put forth in 1964 through two theorems namely, the Hohenberg-Kohn theorems, which tie properties of a many body system to its ground state electron density[9]. Theorem one states that "*The ground state energy from Schrodinger's equation is a unique functional of the electron density"*. The second theorem states that "*The electron density that minimizes the energy of the overall functional is the true electron density corresponding to the full solution of the Schrodinger's equation"*[10,11]. A functional is defined as a function of another function. In DFT, these are the functionals of the spatially dependent electron density.

These two theorems when published, although proven rigorously, were not accompanied by a viable method to solve either electron density or the ground state energy. The ideas put forth by Hohenberg and Kohn were further developed in the Kohn-Sham (KS) equations in 1965 where the many-body problem is mapped to a fictitious system

where noninteracting particles move in an external potential[12]. In KS-DFT many-body effects are approximated with an exchange-correlation functional which in principle is exact but no exact functional is known. The electron density can then be solved which then allows for the calculation of the ground state energy that we desire. This method is an iterative method in which the energies are calculated through multiple iterations until the required accuracy is reached.

2.2 Hohenberg-Kohn (HK) Theorems

The foundations of DFT were established by two theorems put forth and proven by Hohenberg and Kohn in 1964[13]. Theorem 1 proves the ability of electron density mapping to a wavefunction while Theorem 2 recasts the variational principle in terms of electron density.

Theorem 1: *The ground state density $n(\vec{r})$ of a system of interacting particles in an external potential V_{ext} uniquely determines the potential V_{ext} up to a constant value.* This means that the ground state density determines the full Hamiltonian except for a constant shift of energy. Thus, all properties of a system can be determined from the ground state density (n_o):

$$n_o \rightarrow \hat{H} \rightarrow \Psi_0 \rightarrow E_0 \tag{2.1}$$

wherein H is the Hamiltonian operator of the system, Ψ_0 is the wavefunction of the ground state corresponding to the state with the lowest energy E_0. Proof of this theorem was done though contradiction by considering two different external potentials that give rise to the same electron density. The central problem of DFT can also be extracted from this formalism by

decomposing the complete ground state energy into its components. As the ground state energy is a functional of the ground state density so must be its components:

$$E_0[n_o(r)] = T_e[n(r)] + E_{ee}[n_o(r)] + E_{ne}[n_o(r)] \quad (2.2)$$

Wherein T_e is the kinetic energy of electrons, E_{ee} is the function for the potential energy due to electron-electron interactions and E_{ne} is the function for the potential energy due to nucleus-electron interactions. The functional for the potential energy due to nucleus-electron interactions is known:

$$E_{ne}[n_o(r)] = \int n_0(r)\, V_{ext} dr \quad (2.3)$$

But neither the functional for kinetic energy of the electrons nor the potential energy due to electron-electron repulsion are known exactly. They are commonly grouped together and called the Hohenberg-Kohn or Universal Functional:

$$F_{HK}[n_o(r)] = T_e[n_o(r)] + E_{ee}[n_o(r)] \quad (2.4)$$

Finding this exact functional would allow for DFT to be exactly solvable allowing the determination of all properties of a system just from electron density. Because the form of $F_{HK}[n_o]$ is not known, approximations have to be made to solve this problem. Theorem 2 illustrates a cornerstone of these approximations.

Theorem 2: *For any external potential V_{ext} there exists a function $E[n]$. The global minimum of $E[n]$ is given by the ground state density $n_0(\vec{r})$.* This can be written as:

$$\int n_{trial}(r)\, V_{ext} dr + F_{HK}[n_{trial}(r)] = E_{trial} \geq E_0 = \int n_0(r)\, V_{ext} dr + F_{HK}[n_0(r)] \quad (2.5)$$

Where the equality holds when the trial density ($n_{trial}(r)$) is identical to the true ground state density. Like the variational principle, minimization of energy allows for the

determination of the true ground state density. Even with the variational principle in terms of electron density, the approximations of the Universal Functional were not known until the 1965 Kohn-Sham ansatz which allowed (2.5) to be solved. There are forms of DFT known as orbital-free DFT that do not use this ansatz, but these will not be considered.

2.3 Kohn-Sham (KS) Ansatz

The KS ansatz puts the HK theorems into practical usage by approximating the Universal Functional. Due to the success of KS, Walter Kohn was awarded the Nobel prize in Chemistry in 1998[37]. The Kohn-Sham equation can be written as:

$$((-\hbar^2/2m)\,\nabla^2 +)\,V_{ext}(\mathrm{r}) + V_{\mathrm{H}}(\mathrm{r}) + V_{\mathrm{XC}}(\mathrm{r}))\,\psi_{KS}(\mathrm{r}) = \varepsilon_{\mathrm{i}}\,\psi_{KS}(\mathrm{r}) \qquad (2.6)$$

wherein ψ_{KS} is the Kohn-Sham orbital and ∇ is called as the slater determinant.

Kohn-Sham eigenvalues obtained from solving the single-electron wavefunctions ε_i are not for the original many-body system and therefore have no physical meaning. They are not energies to add or subtract from the original many-body problem as the total energy of the system is not equal to the sum of the energies of the occupied single-electron orbitals. These eigenvalues have meaning just in KS theory. This means the non-interacting system is set up and KS equations are solved iteratively in order to find the ground state density by minimizing the eigenvalues which have no physical meaning[36].

2. 4 Doping

Doping is the process of adding an impurity element to a chemical material to alter its original properties, for instance electrical or optical properties. This impurity element is called a dopant or doping agent[38]. The amount of dopant that needs to be added to cause changes is generally very low. When a dopant is added to a crystalline substance, the dopant atom gets incorporated into the crystal lattice. For our research, we add dopants on the surface of the wollastonite crystal to see if they can assist the thermodynamic formation of oxygen vacancies on wollastonite surfaces. There are several trivalent dopants that can be added such as Al^{3+}, Ga^{3+}, In^{3+}, Fe^{3+}, Sc^{3+}, Y^{3+}, Gd^{3+}, La^{3+} and tetravalent dopants such as Ge^{4+}, Ti^{4+}, Sn^{4+}, Zr^{4+} and Ce^{4+}. Among these many possible options for dopants, we choose the trivalent Al^{3+} dopant as they have been shown to be favorable[14]. In addition, the abundance and availability certainly favor the consideration of Al^{3+} dopants. The basic idea is to replace two silicon (Si^{4+}) atoms with two Al^{3+} dopants. In $CaSiO_3$, doping silicon with trivalent dopants result in oxygen vacancies to maintain the defect charge equilibria. For instance, the defect reaction that governs the addition of Al^{3+} dopants to Si^{4+} can be expressed in Kröger–Vink notation as:

$$Al_2O_3 \xrightarrow{SiO_2} 2Al'_{Si} + V_O^{\cdot\cdot} + 3O_O^{\times} \qquad (2.7)$$

where $V_O^{\cdot\cdot}$ represents an oxygen vacancy. This relationship indicates that the substitution of two Si^{4+} ions with Al^{3+} dopants ions on the cation sublattice will result in an oxygen vacancy on the anion sublattice. Such oxygen vacancies are pervasive in doped metal oxides.

Chapter 3 – Computational Method

3.1 Supercells

Wollastonite ($CaSiO_3$) most commonly crystallizes in the triclinic system with space group P1[15]. The unit cell contains two apex-to-apex joining tetrahedra and the silicon-oxygen tetrahedron with one edge parallel to the chain direction in the *b*-axis. Unit cells were obtained from the Materials Project[41] and validated against experimental results[15,16-18]. Experimental lattice constants of the unit cells were a = 7.94 Å, b = 7.32 Å, and c = 7.07 Å with six formula units per unit cell for a total of 30 atoms[19]. Supercells were constructed from layers of wollastonite with three-dimensional periodic boundary conditions (Born– von Karman). Supercells for (100), (010), and (001) surface slabs contained 240 atoms (48 calcium, 48 silicon and 144 oxygen) with 2 × 2 × 2 periodicity built from the unit cell. No evidence of surface reconstructions has been reported in experiments. As a result, we model the wollastonite surfaces with optimized truncated bulk surfaces, which is similar to the approach in literature studies[20,21,22,23,24,36]. To mimic the surface, a vacuum of 15 Å was added along the *z*-axis (normal to the surface) between the supercell slabs. Essentially, for all the slab models, the two surfaces are separated by roughly 15 Å, ensuring that the interaction between the two surface layers is minimal. Constructed models are stoichiometric; prior to further optimization the two surfaces of the slab have the same initial atomic structure due to periodic boundary conditions. We use two layers in the surface model to minimize the calculation time in VASP. Electronic and Structural Analysis (VESTA) package was utilized for creation of supercells along with the visualization of electronic and charge density structures[25,26].

The side and top views of the created supercells are shown for each surface in the **Figure 1**.

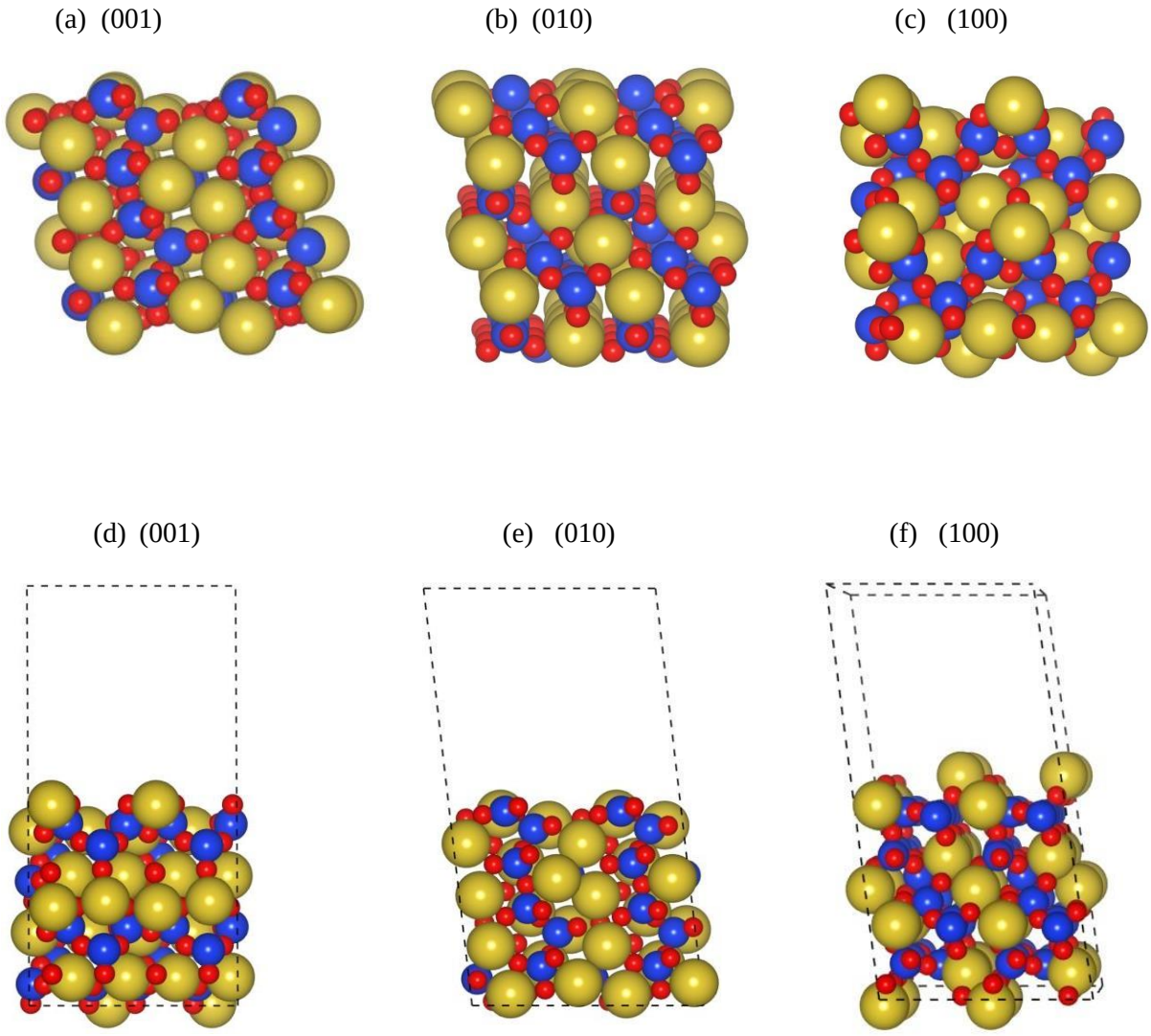

Figure 1. *For geometrically optimized surface slabs, normal (top) views of (001), (010), and (100) surfaces are given in (a), (b), and (c) respectively. Side views of these surfaces are given in (d), (e), and (f). Side view displays the 15 Å vacuum layer along the z-axis and the intricate stacking of atomic planes along with the silicate chains in the [010] direction characteristic of the wollastonite crystal. Gold, blue, and red spheres represent calcium, silicon, and oxygen atoms, respectively*[36].

3.2 VASP

All electronic structure calculations were done using DFT implemented in VASP, the *Vienna ab-initio Simulation Package*, a Fortran program written for atomistic modeling from first principles[27-30]. VASP allows solving the many-body Schrödinger equation within a Hartree-Fock (HF) or DFT framework in order to determine the electronic structure of a system[31]. VASP can take a variety of input files and output a variety of files based on properties that are being studied. The input files used were INCAR, POSCAR, POTCAR and KPOINTS. Output files includes the CONTCAR, OUTCAR, CHGCAR, DOSCAR and OSZICAR. Further information on usage of VASP can be found in VASP the Guide[32]. Parameters used matched those that gave convergence in a similar system[33].

3.2.1 INCAR

The INCAR file is the main input file and controls most of the parameters that can be changed during a calculation. Different flags are used to set parameters:

- ISTART= 0, Begins the calculation from the start – can be set to read wavefunctions from WAVECAR file if restarting or rerunning a system.
- ICHARG = 2, Constructs initial charge density from superposition of atomic charge densities.
- ISPIN=2, Spin polarized calculations are performed.
- GGA=PE, Sets the approximation for the XC function to the PBE function[34,35].

- ISIF=4, Calculates stress tensor along with forces when optimizing geometry, also sets degrees of freedom when optimizing geometry to ionic positions and cell shape while keeping cell volume constant.
- IBRION=2, Ionic positions and cell shape are updated using a conjugate-gradient algorithm.
- POTIM=0.3, Scaling factor for how much the conjugate gradient algorithm updates ionic positions.
- NSW=200, sets geometry iterations to a maximum of 200 unless forces are less than a default of 0.02 eV/Å on each atom.
- LREAL=Auto, Projector augmented wave (PAW) operators are evaluated in real space.
- ISMEAR=0, Gaussian smearing of electron occupancy in orbitals.
- SIGMA=0.3, Width of electron smearing.
- ENCUT=400, Plane wave cutoff in eV.

All other parameters were set to default.

3.2.2 POSCAR

The POSCAR file provides initial ionic positions for the system. The first line is a comment line. The second line is a universal scaling factor which scales all lattice vectors and all ionic coordinates. The third, fourth and fifth lines are the lattice vectors defining the unit cell of the system. The sixth line provides the atomic symbols of the chemical elements of the system. The seventh line is the corresponding numbers of atoms for elements written in the sixth line. The eighth line is an optional line that allows for selective dynamics to be switched on, this mode allows control of whether the respective coordinate(s) of each atom will be allowed to change during the ionic relaxation. In this

work, selective dynamics was not used. The eighth/ninth line specifies whether the coordinates of atoms are written in Cartesian or in direct (fractional) coordinates. The next lines are the three coordinates for each atom in the unit cell. Initial velocities can be provided if performing molecular dynamics after the ionic positions.

3.2.3 POTCAR

The POTCAR file includes the pseudopotentials (PAW potentials) of all the elements in the system seen in line six of the POSCAR; these pseudopotentials are provided by VASP. The POTCAR also contains the maximum and minimum energy values needed to approximate the wavefunction for each element using plane waves. The ENCUT=400 flag from the INCAR file comes from the maximum value of the oxygen atoms in the system.

3.2.4 KPOINTS

The KPOINT file indicates the coordinates and weights of k-points in the Brillouin zone for sampling. In our case, an automatic k-mesh is generated using the Monkhorst-Pack method. A 10 × 10 × 10 and 2 × 2 × 1 mesh was used to relax the bulk and the surface structure, respectively – the smaller numbered mesh was used

3.2.5 CONTCAR

The CONTCAR file has the same file format as the POSCAR – it holds updated ionic positions after each geometry optimization.

3.2.6 OUTCAR

The main output file of calculations is the OUTCAR, it details everything that occurs in the calculation. It contains information read from the input files, symmetry

analysis of the system, information on analyzed and detailed job information; lattice, k- points, forces, stress and ionic positions information for each ionic step; basis set and pseudopotential information along with detailed information of each electronic step; eigenvalues, charge and timing information.

3.2.7 CHGCAR

The CHGCAR file has the same file format as the POSCAR – it holds updated ionic positions after each geometry optimization while also including charge density and PAW occupancies.

3.2.8 DOSCAR

The DOSCAR file contains the DOS or density of states and the integrated DOS of each ion in the system. Calculated DOS can be spin-polarized and decomposed into orbitals by setting flags in the INCAR.

3.2.9 OSZICAR

The OSZICAR file is a simplified version of OUTCAR file which includes information about each electronic step. Iteration count, total energy and change of total energy can be found to assess convergence.

Chapter 4 – Results

4.1 Oxygen vacancy formation energy in undoped wollastonite

To understand the thermodynamic stability of oxygen vacancies, we need to calculate the oxygen vacancy formation energies in the wollastonite unit cell. For this purpose, we consider only oxygen vacancies formed on the surface of wollastonite since our ultimate aim is to enhance the reactivity of the wollastonite surfaces through incorporation of vacancies and dopants. Although subsurface oxygen vacancies are likely to occur, we focus strictly on surface vacancies so as to investigate surface reactivity.

To calculate the oxygen vacancy formation energy, we use the $2 \times 2 \times 2$ wollastonite supercells obtained as described in section 3.1. We remove one oxygen atom from the entire supercell as shown in **Figure 3**. We then obtain the relaxed structure of this supercell from VASP by using the input files mentioned in section 3.2. We repeat this process for a different site of oxygen vacancy (asymmetric from the one mentioned above) and for different low-index wollastonite surfaces. The top view of the supercells before and after removing one oxygen atom for (010) and (100) surfaces can be found in the **Appendix (Figures A.1 - A.4)**.

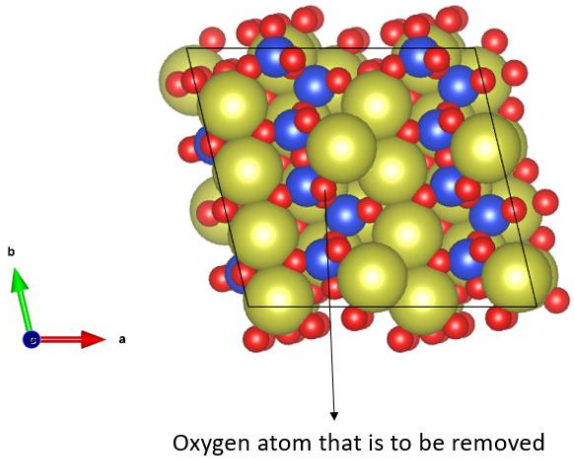

***Figure 2**. Top view of the (001) surface showing the oxygen atom that will be removed from wollastonite.*

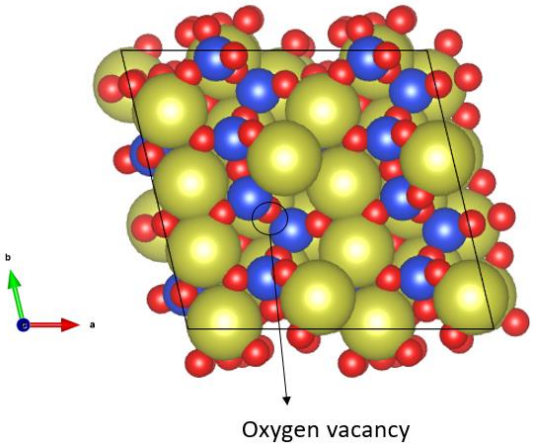

***Figure 3**. Top view of the (001) surface showing the missing oxygen atom (vacancy).*

The total energy is obtained from DFT calculations performed using VASP, an image of which is show in **Figure 4** for the (001) surface. The lowest energy is considered to be the total energy of the supercell.

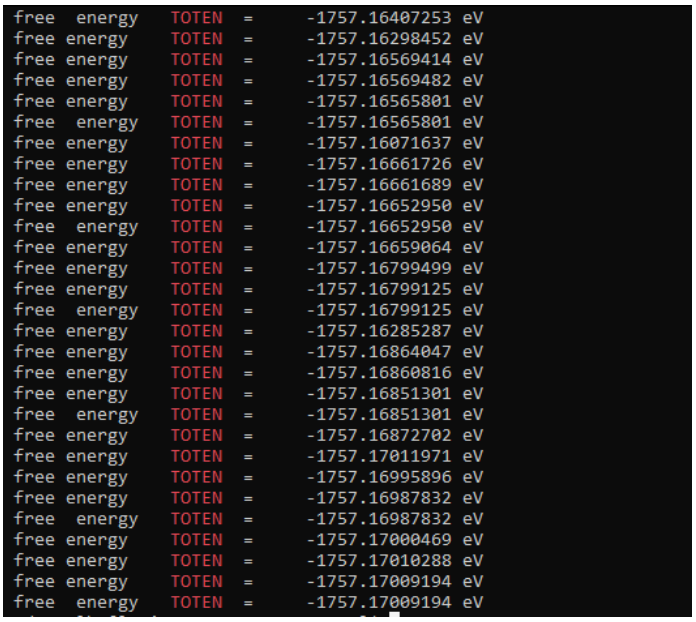

Figure 4*. Total energy of wollastonite for (001) surface can be extracted from the OUTCAR file using the command "grep TOTEN OUTCAR". Each line represents different iterations and the lowest energy among them at the bottom of the figure is used for the calculations.*

The oxygen vacancy formation energy is then calculated by using the formula[40]:

$$E_{(f\ vac)} = E(cell_{\ vac}) + \tfrac{1}{2}\, E(O_2) - E(cell) \qquad (4.1)$$

wherein $E(cell_{\ vac})$ is the total energy of the supercell with oxygen vacancy, $E(O_2)$ is the total energy of the ground state of an oxygen molecule and E(cell) is the total energy of the supercell without oxygen vacancy.

Figures 5, 7 and **9** show the sites chosen for the oxygen vacancy formation energy calculations for the surfaces (001), (010) and (100) respectively. **Figures 6, 8** and **10** show the supercells after the formation of an oxygen vacancy for the surfaces (001), (010) and (100) respectively.

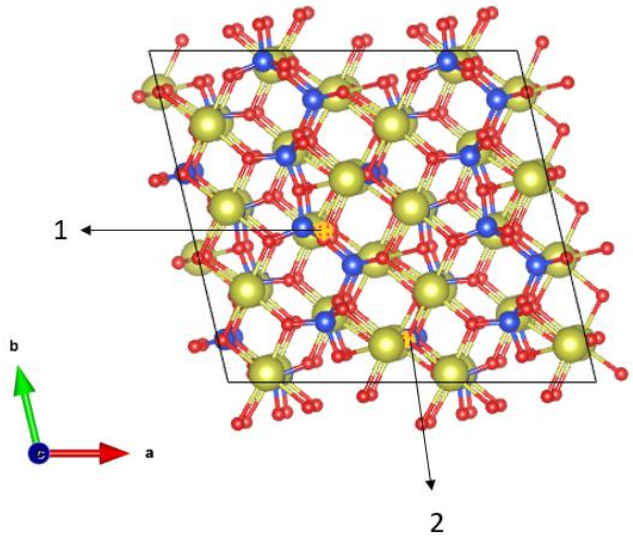

***Figure 5a**. Top view of the (001) surface showing the site numbers 1 and 2 in the ball-and-stick model of wollastonite. The sites were chosen in such a way that they are located on the surface and have different symmetries.*

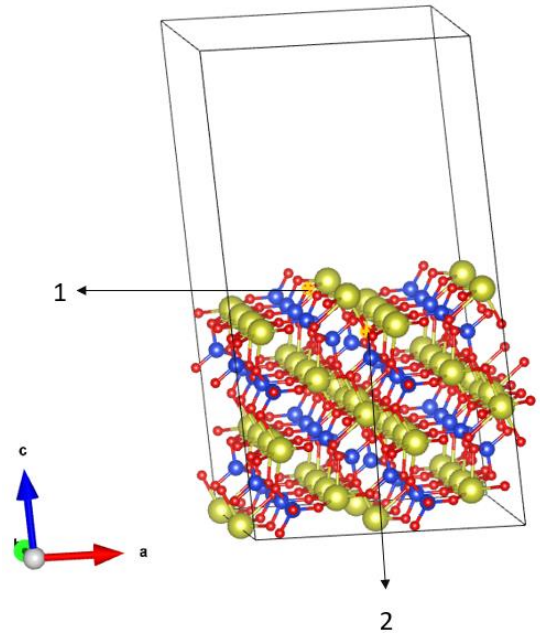

***Figure 5b**. Side view of the ball-and-stick model of the supercell showing the site numbers 1 and 2 for the (001) surface.*

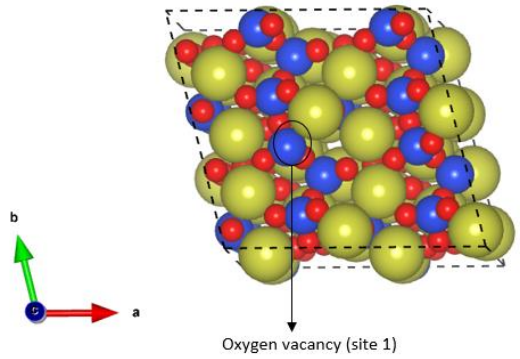

Figure 6a. Top view of wollastonite after the formation of oxygen vacancy at site 1 for (001) surface. This structure is referred to as the relaxed structure that we get from the CONTCAR file after DFT calculations are performed in VASP.

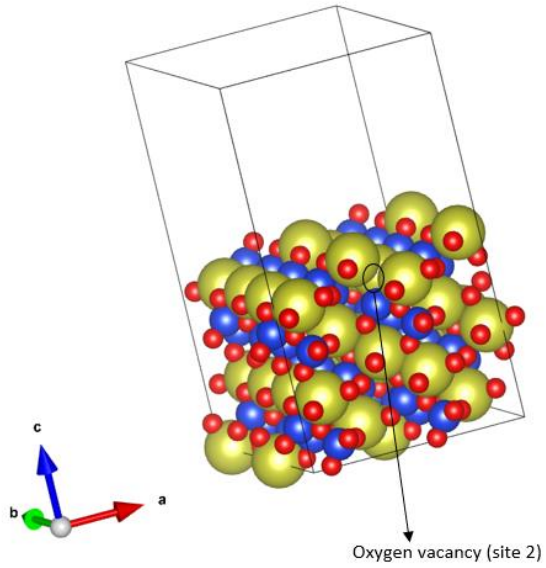

Figure 6b. Side view of wollastonite after the formation of oxygen vacancy at site 2 for (001) surface.

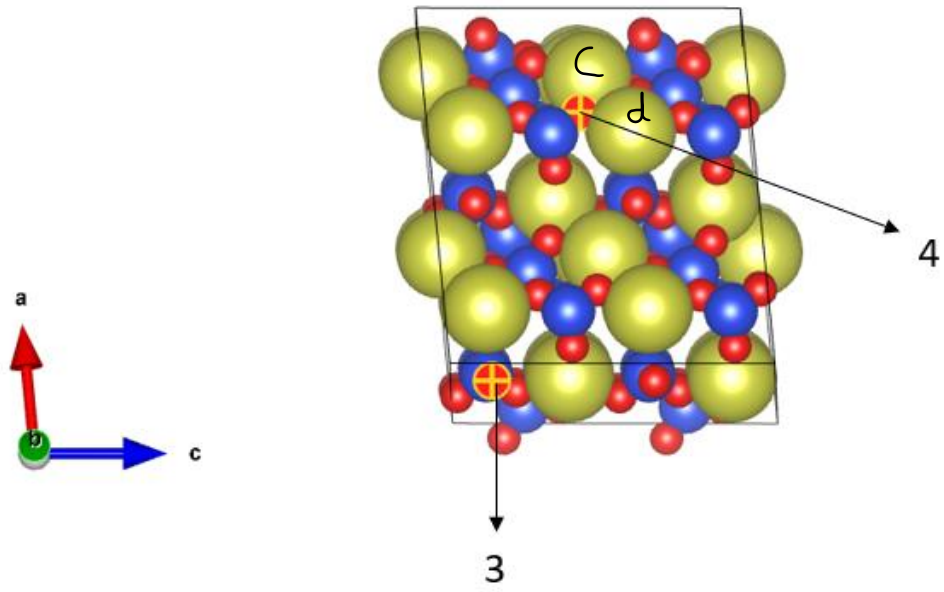

Figure 7*. Top view of the (010) surface showing the site numbers 3 and 4. The calcium atoms bonded to the oxygen atom at site 4 are named 'c' and 'd' and these atoms will be referred to later in this section.*

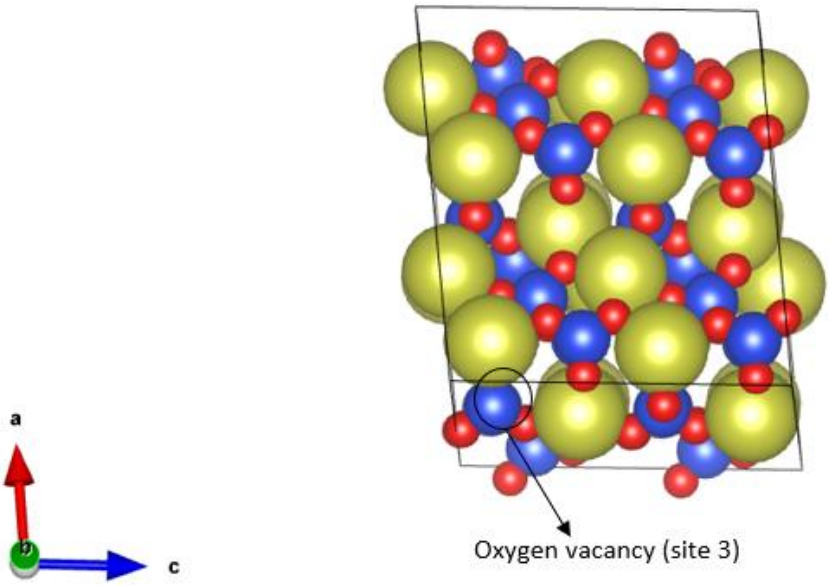

Figure 8a*. Top view of the (010) surface after the formation of oxygen vacancy at site 3.*

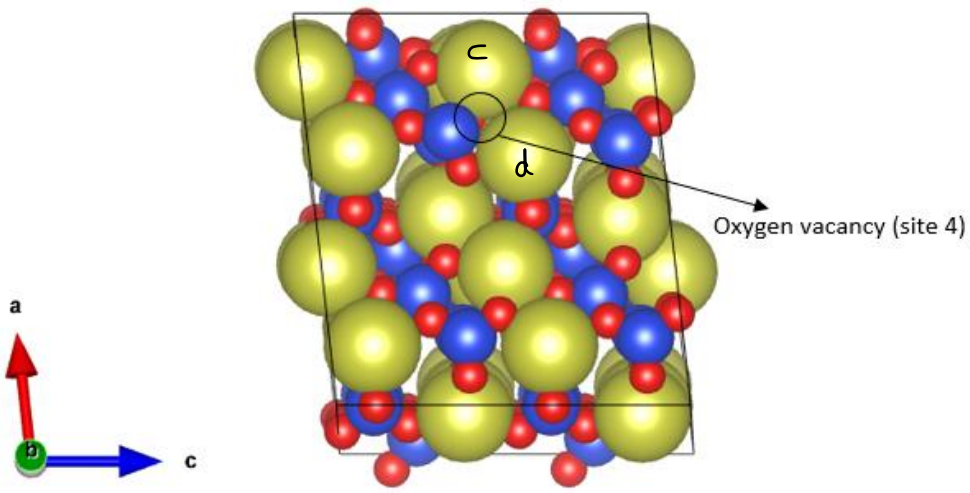

***Figure 8b**. Top view of the (010) surface after the formation of oxygen vacancy at site 4. The calcium atoms marked 'c' and 'd' will be referred to later in this section.*

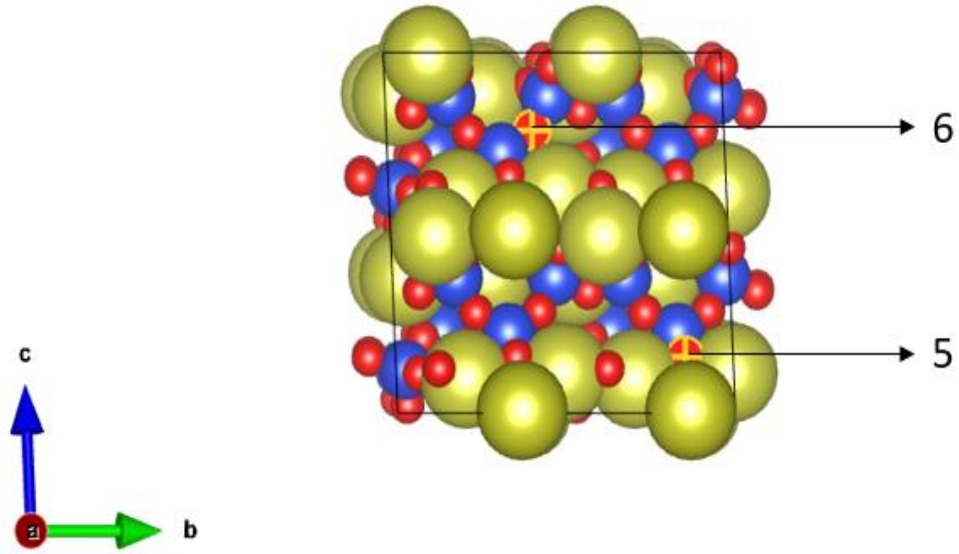

***Figure 9**. Top view of the (100) surface showing the site numbers 5 and 6.*

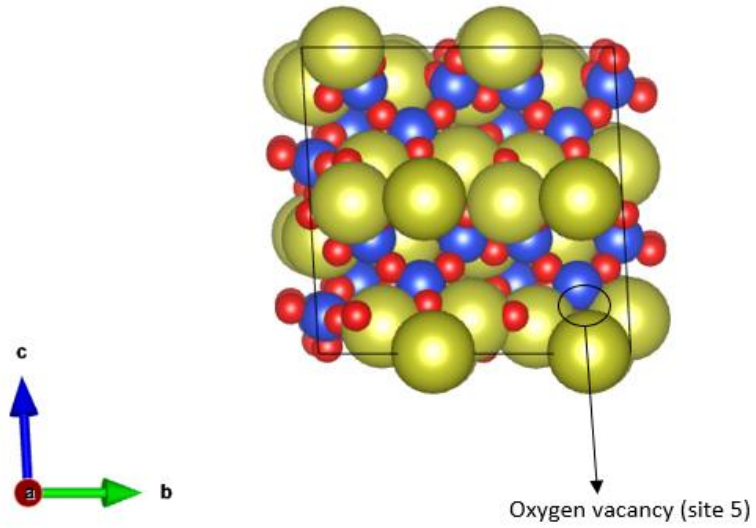

***Figure 10a**. Top view of the (100) surface after the formation of oxygen vacancy at site 5.*

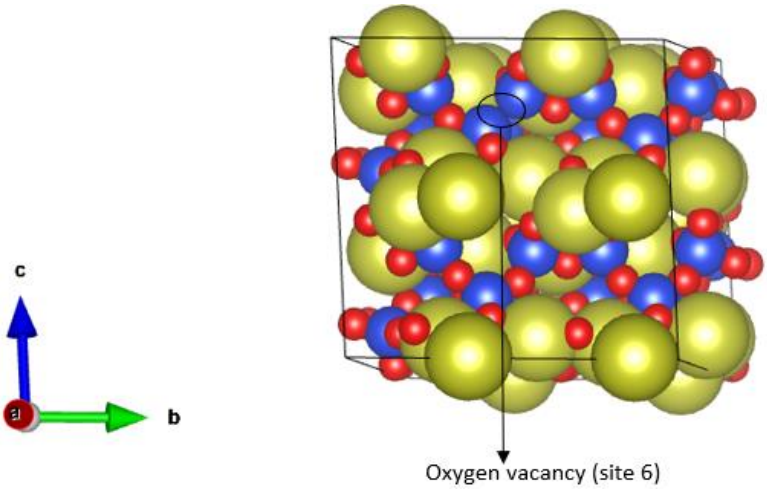

***Figure 10b**. Top view of the (100) surface after the formation of oxygen vacancy at site 6.*

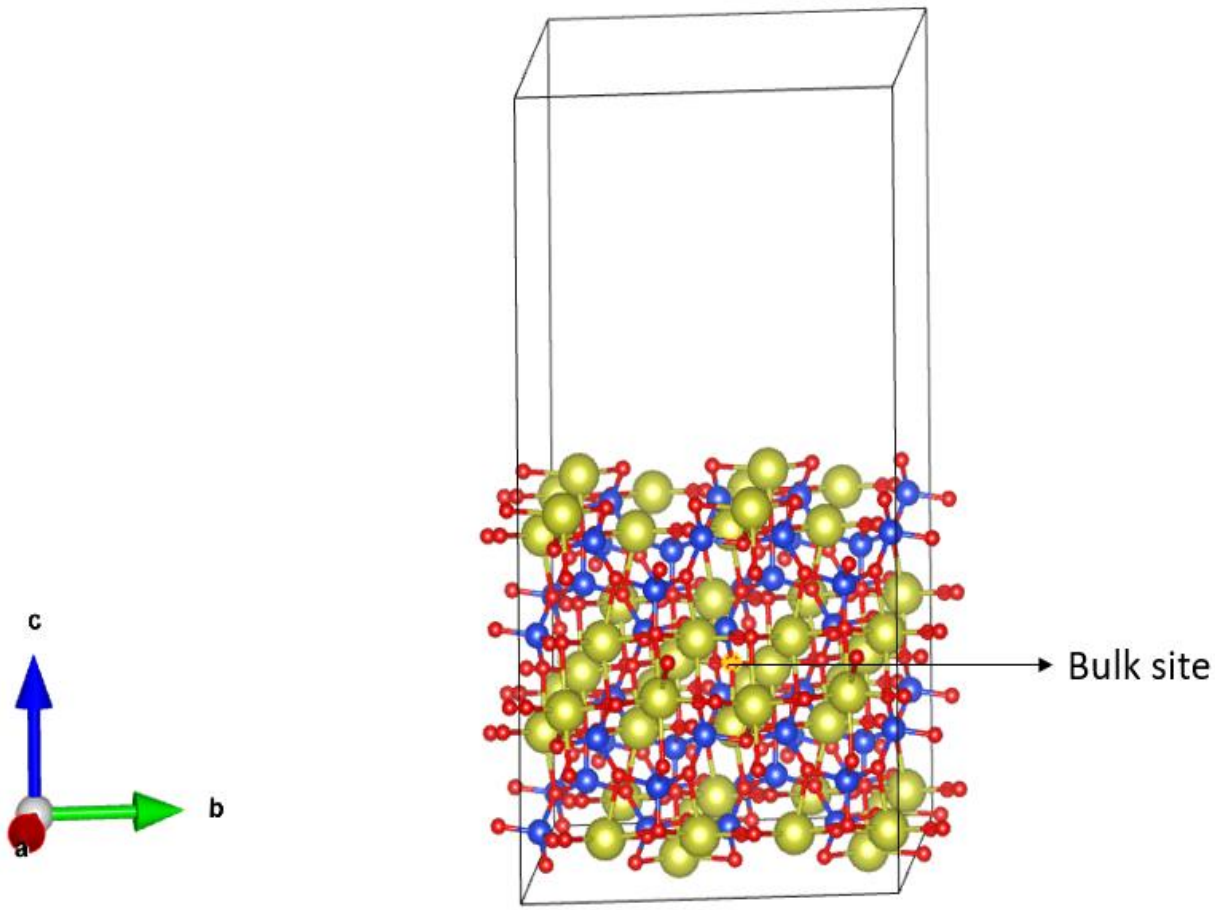

Figure 11. *Side view of the ball-and-stick model showing the oxygen atom in the bulk of the supercell. This is to draw comparison with the surface sites.*

Table 1. *Total energies of the supercells having different oxygen vacancy sites and surfaces of wollastonite. The energy difference between various models gives the net magnitude of surface stability.*

Surface	Site number	$E(cell_{vac})$ in eV
(001)	1	-1757.17009194
(001)	2	-1756.38665584
(010)	3	-1756.74654019
(010)	4	-1757.90245041
(100)	5	-1751.50898179
(100)	6	-1751.96211998

The following values were available from Brian Luan's thesis work[36]:

$E(O_2)$ = -9.860633 eV. This value of $E(O_2)$ will be used for all the subsequent calculations.

E(cell) for (001) surface = -1767.060695 eV

E(cell) for (010) surface = -1767.00756331 eV

E(cell) for (100) surface = -1761.48113031 eV

Using the above data and values from the **Table 1**, we find the oxygen vacancy formation energies at two different sites for each surface of the wollastonite supercell.

Table 2*. Using the total energies values from Table 1, oxygen vacancy formation energies are calculated at two different sites for (001), (010) and (100) surfaces of wollastonite.*

Surface	Site number	$E_{(f\ vac)}$ in eV
(001)	1	4.96
(001)	2	5.74
(010)	3	5.33
(010)	4	4.17
(100)	5	5.04
(100)	6	4.59

In simple terms, oxygen vacancy formation is the removal of an oxygen ion in the material, which is a fairly common defect observed in metal oxides, especially in experiments. We observe that the oxygen vacancy formation energies are all positive. It implies that the oxygen vacancy formation at the surface of the wollastonite is an endothermic process, which means some external energy is required for the vacancy to be formed and it's not naturally occurring. This is further supplemented by measuring the interatomic distance between the calcium atoms bonded to the oxygen atom before and after the formation of oxygen vacancy. For this purpose, we choose the oxygen atom at site 4 which has the lowest oxygen vacancy formation energy. Initially, before the formation of an oxygen vacancy at site 4 (shown in Figure 6), the interatomic distance between

the two calcium atoms ‘c’ and ‘d’ bonded to the oxygen atom at site 4 is approximately 3.83 Å. After the formation of the oxygen vacancy at site 4, the interatomic distance between the calcium atoms ‘c’ and ‘d’ increases to approximately 4.02 Å. This tells us that the interatomic Ca-O bonding at the surface of the supercell is altered after oxygen vacancy formation. As such, the interatomic Ca-Ca distance is smaller since both the calcium atoms are held together by the oxygen atom between them. Once both the Ca-O bonds break during the formation of an oxygen vacancy, the calcium atoms repel each other leading to the increase in their interatomic distance. This is the reason why the formation of oxygen vacancy isn’t naturally feasible due to the significant bonding strength between the oxygen and calcium atoms.

We further calculate the oxygen vacancy formation energy in the bulk (as shown in **Figure 11**) of the (001) wollastonite supercell and its value turns out to be 5.65 eV ($E_{(f\ vac,\ bulk)}$). Comparing this value with all the oxygen vacancy formation energies in Table 2, we can observe that except for one value, all the other values in **Table 2** are lower than $E_{(f\ vac,\ bulk)}$. This means that the formation of oxygen vacancies is more favorable at the surface than in the bulk of the wollastonite.

4.2 Oxygen vacancy formation energies in doped wollastonite

We now investigate if doping wollastonite will aid in the formation of oxygen vacancies without requiring external energy. For this purpose, we dope wollastonite with aluminum (Al^{3+}) atoms. Two silicon (Si^{4+}) atoms on the wollastonite surface are replaced by two aluminum atoms. The silicon atoms chosen are in such a way that they are at first nearest neighbor (1NN) and second nearest neighbor (2NN) with respect to the location of the oxygen vacancy since they are expected to have lower energy configurations.

For calculating the oxygen vacancy formation with doping, we use the following formula:

$$E_{(f\ vac)} = E(Al_{\ vac}) + \tfrac{1}{2}\, E(O_2) - E(Al) \qquad (4.2)$$

wherein $E(Al_{\ vac})$ is the total energy of the aluminum doped supercell with oxygen vacancy, $E(O_2)$ is the total energy of the ground state of an oxygen molecule and E(Al) is the total energy of the aluminum doped supercell without oxygen vacancy. Similar to section 4.1, we carry out all the calculations in 4.2 for the (001), (010) and (100) surfaces of the wollastonite supercell.

4.2.1 Oxygen vacancy formation energies with doping for (1NN, 1NN) locations.

The nearest neighbors are determined by the distance between the oxygen vacancy site and the dopant atom sites, which replace the silicon atoms. Different dopant atom sites were tried and the ones with the least atomic distance between them and the oxygen vacancy site were chosen as the first nearest neighbor (1NN). Nearest neighbor distances can also be directly obtained from bulk wollastonite. However, we used surface models since the surface layer atoms undergo relaxation. We select 2 dopant atom sites at (1NN, 1NN) locations with respect to the oxygen vacancy site to perform the total energy calculations and oxygen vacancy formation energy calculations as shown in the **Figures 12, 13** and **14** for (001), (010) and (100) surfaces, respectively.

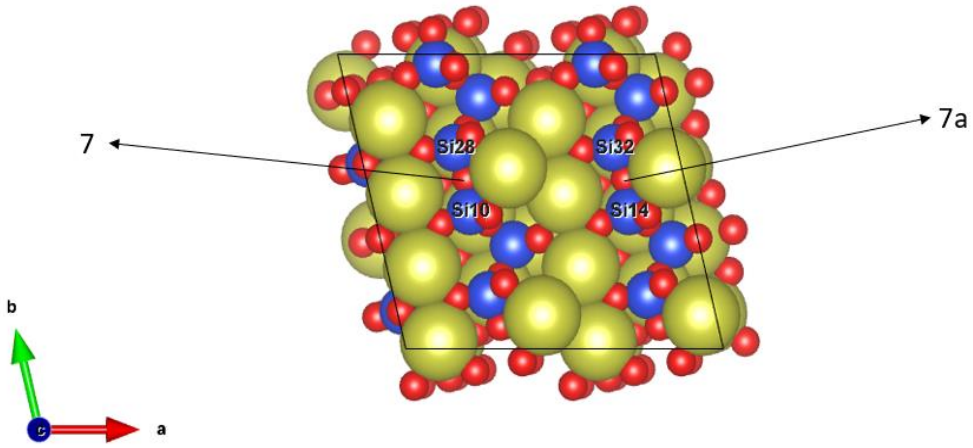

Figure 12*. Top view of the (001) surface showing the sites 7 and 7a. The silicon atoms Si 28 and Si 10 are the first nearest neighbors to the oxygen atom at site 7 i.e they are at 1NN locations with respect to the oxygen atom at site 7.*

It is confirmed that they are the first nearest neighbors via measuring the distance between the silicon atoms (Si 28 and Si 10) and the site 7 oxygen atom that is approximately 1.6 Å. This turns out to be the least possible distance between any silicon atom and oxygen atom residing at the surface of the supercell for the (001) surface. The silicon atoms Si 32, Si 14 and the oxygen atom at site 7a have the same symmetries as the silicon atoms Si 28, Si 10 and the oxygen atom at site 7, respectively.

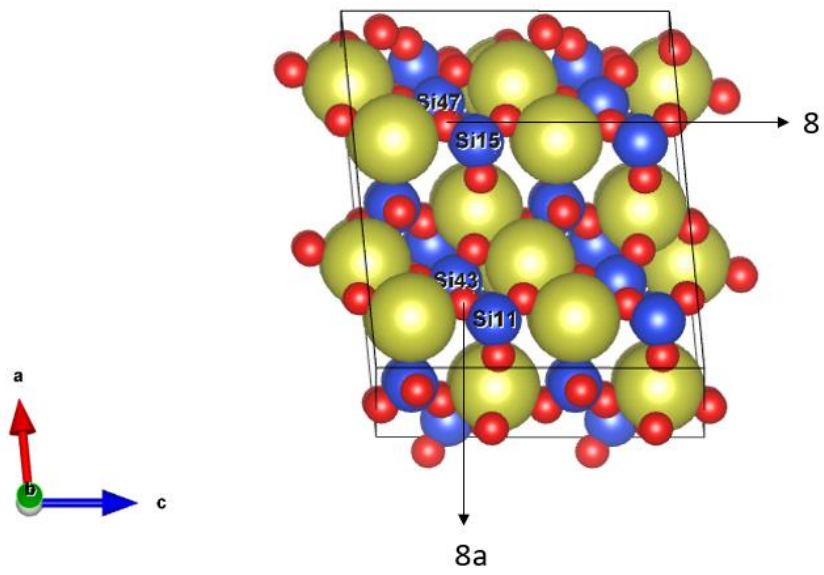

Figure 13*. Top view of the (010) surface showing the sites 8 and 8a. The silicon atoms Si 47 and Si 15 are the first nearest neighbors to the oxygen atom at site 8 i.e they are at 1NN locations with respect to the oxygen atom at site 8.*

It is confirmed that they are the first nearest neighbors via measuring the distance between the silicon atoms (Si 47 and Si 15) and the site 8 oxygen atom that is approximately 1.65 Å. This turns out to be the least possible distance between any silicon atom and an oxygen atom present at the surface of the supercell for the (010) surface. The silicon atoms Si 43, Si 11 and the oxygen atom at site 8a have the same symmetries as the silicon atoms Si 47, Si 15 and the oxygen atom at site 8 respectively.

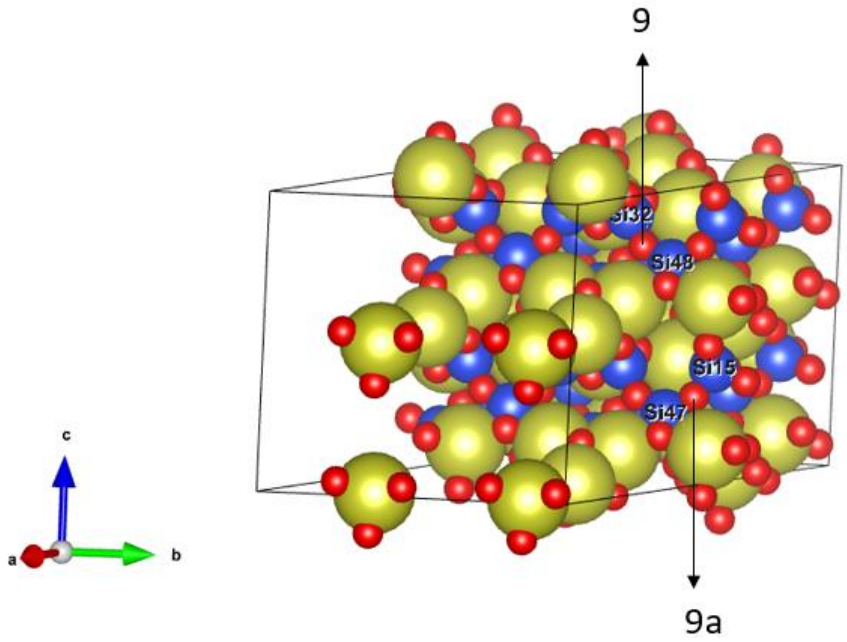

Figure 14*. Top view of the (100) surface showing the sites 9 and 9a. The silicon atoms Si 32 and Si 48 are the first nearest neighbors to the oxygen atom at site 9 i.e they are at 1NN locations with respect to the oxygen atom at site 9.*

It is confirmed that they are the first nearest neighbors via measuring the distance between the silicon atoms (Si 32 and Si 48) and the site 9 oxygen atom that is approximately 1.6 Å. This turns out to be the least possible distance between any silicon atom and an oxygen atom present at the surface of the supercell for the (100) surface. The silicon atoms Si 15, Si 47 and the oxygen atom at site 9a have the same symmetries as the silicon atoms Si 32, Si 48 and the oxygen atom at site 9 respectively.

Table 3. *Total energies of the aluminum doped wollastonite with oxygen vacancy and dopant atom sites at (1NN,1NN) locations with respect to the oxygen vacancy site.*

Surface	Site number	E(Al $_{vac}$) in eV	E(Al) in eV
001	7	-1753.52130371	-1759.06817050
010	8	-1755.52115602	-1759.72239604
100	9	-1750.62096552	-1754.30853509

Figures 15, **16** and **17** show the top view of the supercells after the formation of oxygen vacancy for the (001), (010) and (100) surface, respectively.

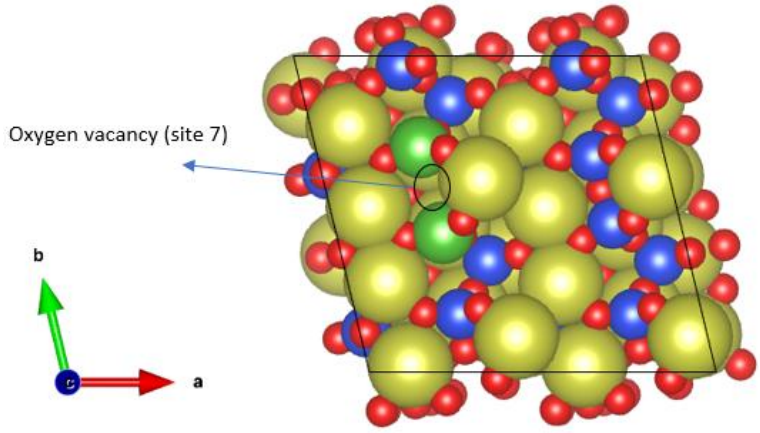

Figure 15*. Top view of the (001) surface after the formation of oxygen vacancy at site 7.*

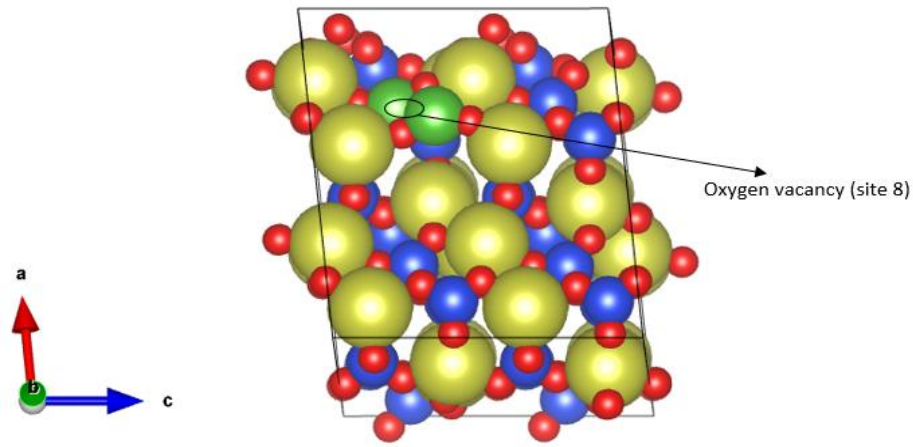

Figure 16*. Top view of the (010) surface after the formation of oxygen vacancy at site 8.*

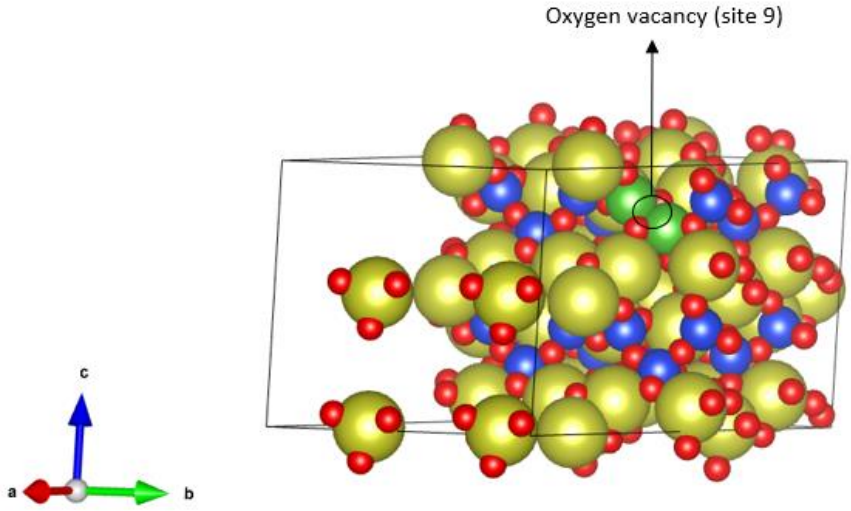

Figure 17*. Top view of the (100) surface after the formation of oxygen vacancy at site 9.*

Table 4. *Using the total energies values from Table 3, oxygen vacancy formation energies are calculated for the aluminum doped wollastonite with the doping locations at (1NN, 1NN) with respect to the oxygen vacancy site.*

Surface	Site number	$E_{(f\ vac)}$ in eV
001	7	0.62
010	8	-0.73
100	9	-1.24

We can now observe that the oxygen vacancy formation energies are lower in values and mostly negative compared to those values obtained in 4.1. The negative values mean that the oxygen vacancy formation is exothermic which implies that the oxygen vacancies are more likely to form on the wollastonite surface in the presence of dopants.

This phenomenon can be further explained using reaction (1.2). In this reaction, the active center in the calcium silicate is the calcium oxide (CaO) that leads to the formation of $CaCO_3$ as follows:

$$CaO + CO_2 \rightarrow CaCO_3 \tag{4.3}$$

Based on this, we can write the $CaSiO_3$ molecule as $CaO.SiO_2$. In the supercell we use, there are 48 such molecules of $CaO.SiO_2$. Now consider two molecules of $CaO.SiO_2$. We can write them as $(CaO.SiO_2)_2$ which in turn can be considered as $(CaO)_2$. $(SiO_2)_2$ or $(CaO)_2$. Si_2O_4. When replacing 2 atoms of silicon with 2 aluminum atoms, what we do practically is replace one atom

of silicon each from 2 molecules of $CaO.SiO_2$. After doping with aluminum, $(CaO)_2$. Si_2O_4 changes to $(CaO)_2$. Al_2O_4.

Since aluminum is only stable in the form of Al_2O_3, in this process, an oxygen atom is expelled from the surface which then creates the imperfection in the crystal as an oxygen vacancy. Thus, the formation of an oxygen vacancy on the surface of the wollastonite crystal is thermodynamically favorable after addition of aluminum dopants. To further confirm this, we perform calculations at different vacancy and dopant locations which will be discussed in the upcoming sections. We find the oxygen vacancy formation energies at different oxygen vacancy sites but with same symmetry as the sites 7,8 and 9 mentioned in 4.2.1. **Figures 12, 13 and 14** show the dopant sites and oxygen vacancy sites 7a, 8a and 9a that have the same symmetry as the sites 7,8 and 9. We then proceed with the similar calculations as in 4.2.1

Table 5. *Total energies of the aluminum doped wollastonite with oxygen vacancy and dopant atom sites at (1NN, 1NN) locations with respect to the oxygen vacancy site. Also, these dopant atom sites have the same symmetry as sites 7, 8 and 9.*

Surface	Site number	E(Al_{vac}) in eV	E(Al) in eV
001	7a	-1753.54046810	-1759.04511902
010	8a	-1755.51644811	-1759.71959183
100	9a	-1750.45225954	-1754.31248032

Figures 18, **19** and **20** show the top view of the wollastonite after the formation of oxygen vacancy for the (001), (010) and (100) surface, respectively.

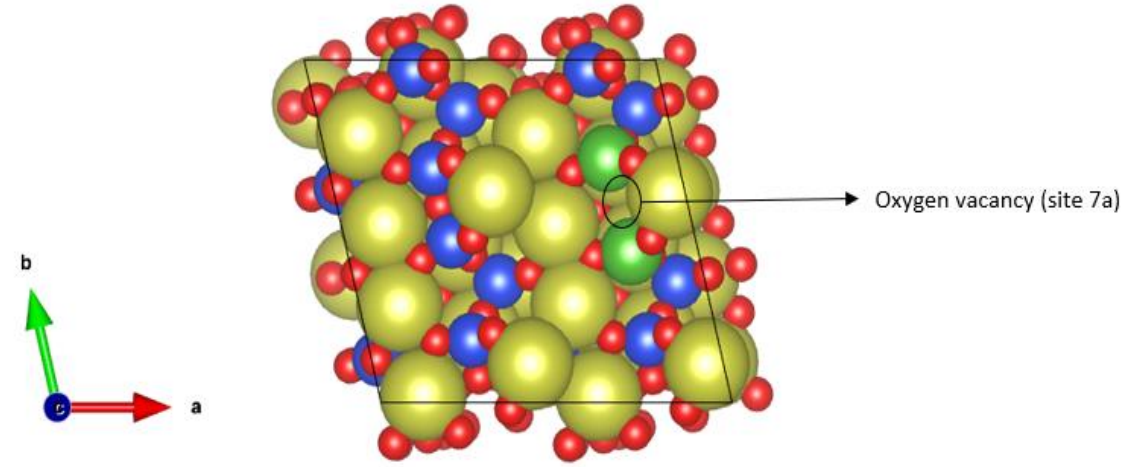

Figure 18*. Top view of the (001) surface after the formation of oxygen vacancy at site 7a.*

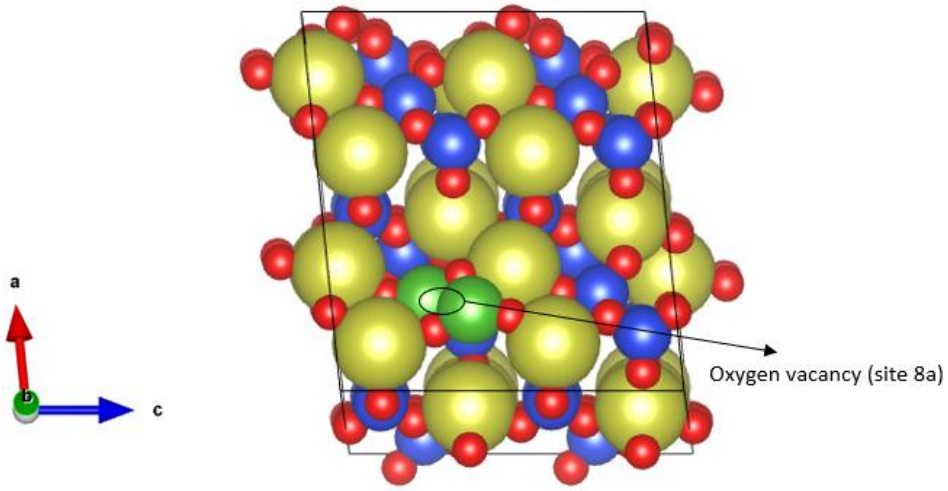

Figure 19*. Top view of the (010) surface after the formation of oxygen vacancy at site 8a.*

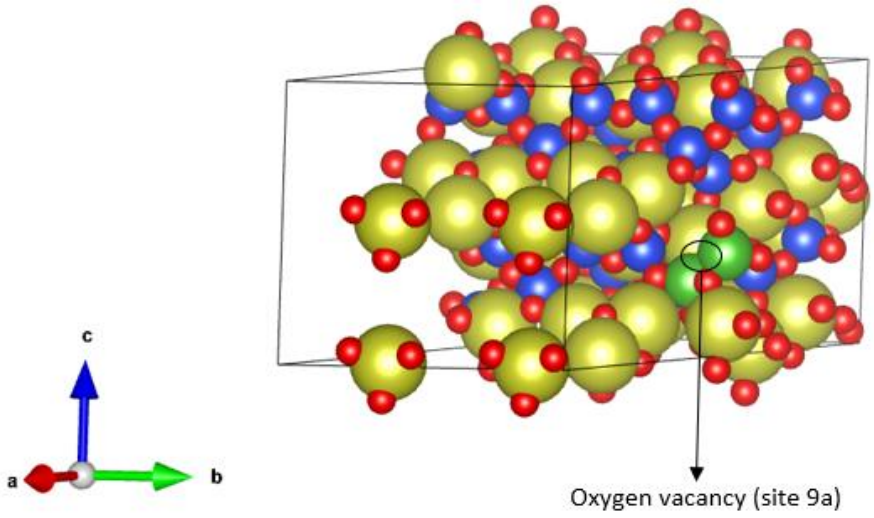

Figure 20*. Top view of the (100) surface after the formation of oxygen vacancy at site 9a.*

Table 6. *Using the total energies values from Table 5, oxygen vacancy formation energies are calculated for the aluminum doped wollastonite with the doping locations at (1NN, 1NN) with respect to the oxygen vacancy site.*

Surface	Site number	$E_{(f\ vac)}$ in eV
001	7a	0.57
010	8a	-0.73
100	9a	-1.07

4.2.2 Oxygen vacancy formation energies with doping for (1NN, 2NN) locations.

In this case, we find the oxygen vacancy formation energies for aluminum doped wollastonite supercell that have the dopant atom sites at 1NN and 2NN locations with respect to the oxygen vacancy site. **Figures 21, 22 and 23** show the dopant atom sites that are at 1NN and 2NN locations with respect to the oxygen vacancy sites for the surfaces (001), (010) and (100) respectively.

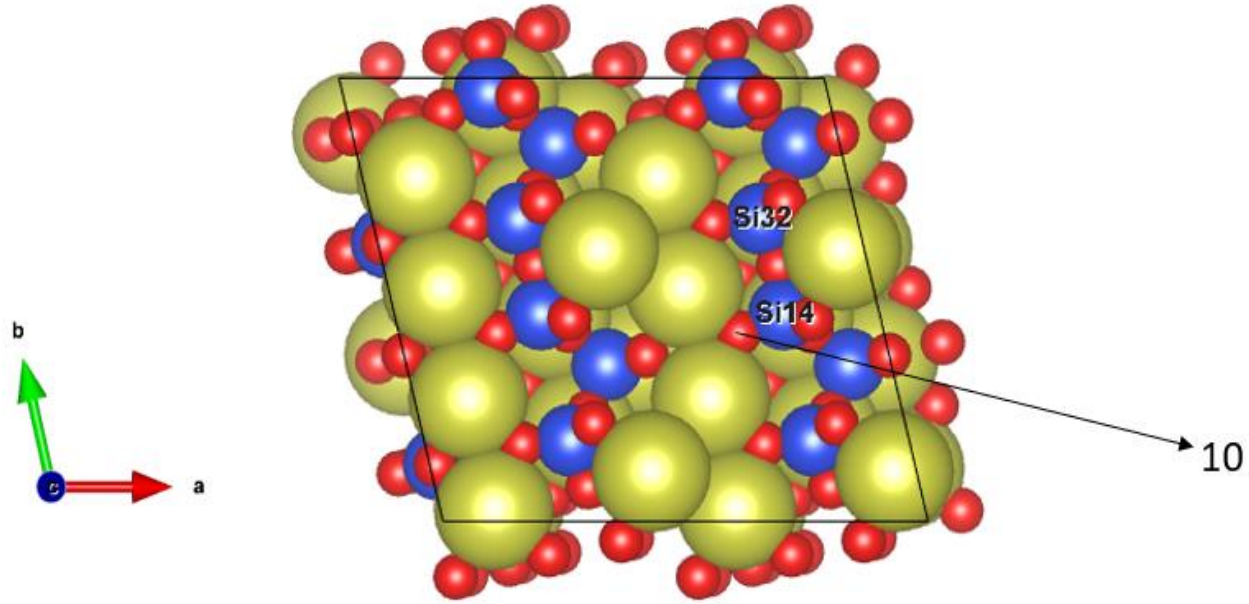

Figure 21. *Top view of the (001) surface showing the site 10. The silicon atom Si 32 is at the 1NN location, and the silicon atom Si 14 is at the 2NN location (second nearest neighbor) with respect to the oxygen atom at site 10.*

The distance between the silicon atom Si 14 and the site 10 oxygen atom is approximately 1.6 Å. This turns out to be the least possible distance between any silicon atom and an oxygen atom present at the surface of the supercell for the (001) surface and hence, it is confirmed that it is at the 1NN location with respect to the site 10 oxygen atom. The distance between the silicon atom

Si 32 and the site 10 oxygen atom is approximately 3.7 Å. This turns out to be the second lowest possible distance between any silicon atom and an oxygen atom present at the surface of the supercell for the (001) surface and hence, it is confirmed that it is at the 2NN location with respect to the site 10 oxygen atom.

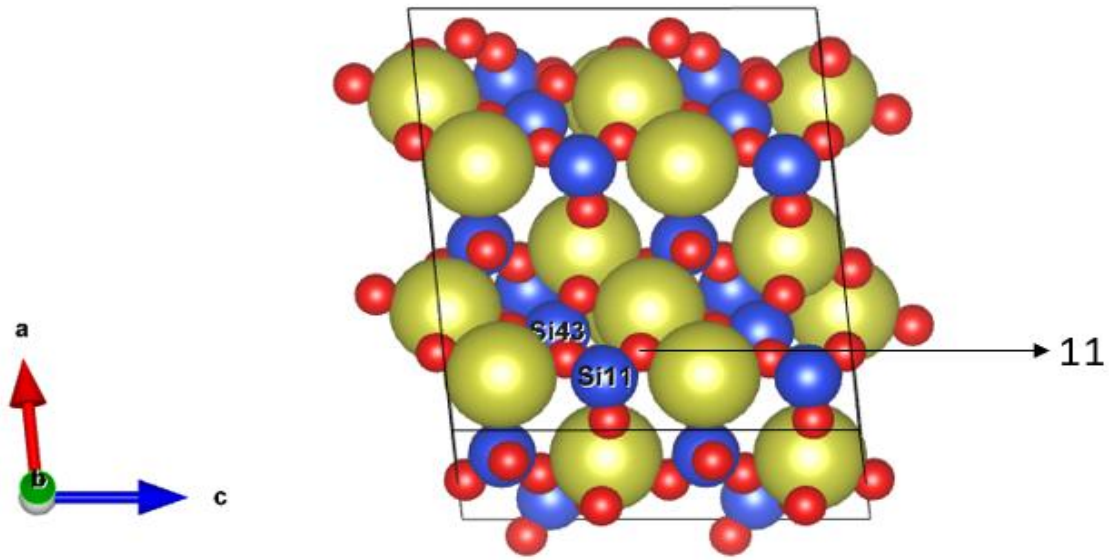

Figure 22. *Top view of the (010) surface showing the site 11. The silicon atom Si 11 is at the 1NN location, and the silicon atom Si 43 is at the 2NN location (second nearest neighbor) with respect to the oxygen atom at site 11.*

The distance between the silicon atom Si 11 and the site 11 oxygen atom is approximately 1.6 Å. This turns out to be the least possible distance between any silicon atom and an oxygen atom present at the surface of the supercell for the (010) surface and hence, it is confirmed that it is at the 1NN location with respect to the site 11 oxygen atom. The distance between the silicon atom Si 43 and the site 11 oxygen atom is approximately 3.4 Å. This turns out to be the second lowest possible distance between any silicon atom and an oxygen atom present at the surface of

the supercell for the (010) surface and hence, it is confirmed that it is at the 2NN location with respect to the site 11 oxygen atom.

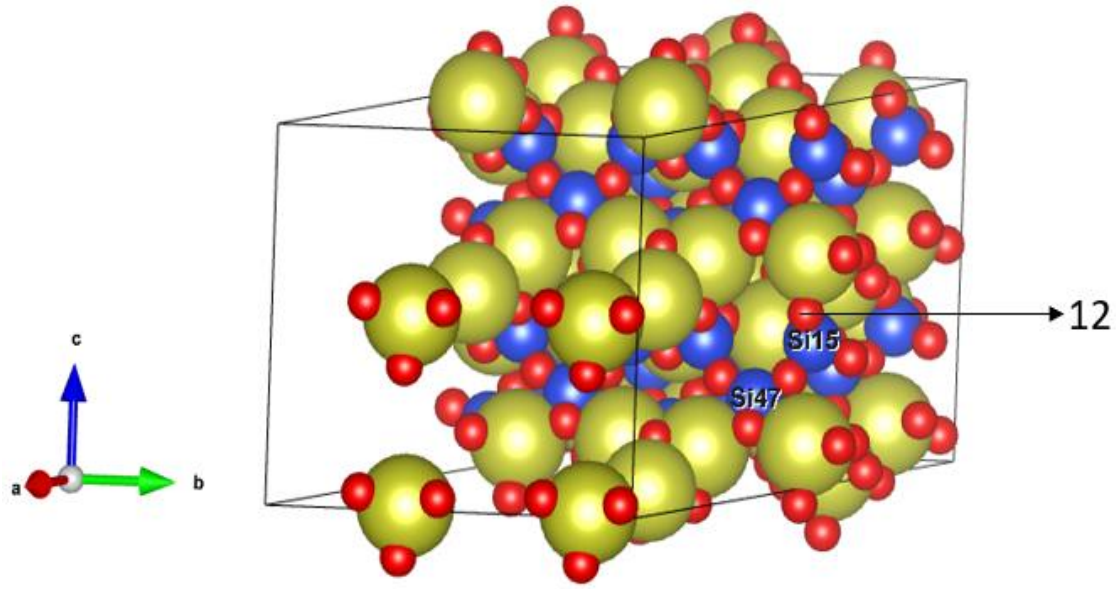

Figure 23. *Top view of the (100) surface showing the site 12. The silicon atom Si 15 is at the 1NN location, and the silicon atom Si 47 is at the 2NN location (second nearest neighbor) with respect to the oxygen atom at site 12.*

The distance between the silicon atom Si 15 and the site 12 oxygen atom is approximately 1.6 Å. This turns out to be the least possible distance between any silicon atom and an oxygen atom present at the surface of the supercell for the (100) surface and hence, it is confirmed that it is at the 1NN location with respect to the site 12 oxygen atom. The distance between the silicon atom Si 47 and the site 12 oxygen atom is approximately 4 Å. This turns out to be the second lowest possible distance between any silicon atom and an oxygen atom present at the surface of the supercell for the (100) surface and hence, it is confirmed that it is at the 2NN location with respect to the site 12 oxygen atom.

Table 7. *Total energies of the aluminum doped wollastonite with oxygen vacancy and dopant atom sites at (1NN,2NN) locations with respect to the oxygen vacancy site.*

Surface	Site number	E(Al $_{vac}$) in eV	E(Al) in eV
001	10	-1754.30795447	-1759.04511902
010	11	-1754.36435960	-1759.71959183
100	12	-1749.50995349	-1754.31248032

The **Figures 24**, **25** and **26** show the top view of the supercells after the formation of oxygen vacancy for the (001), (010) and (100) surfaces, respectively.

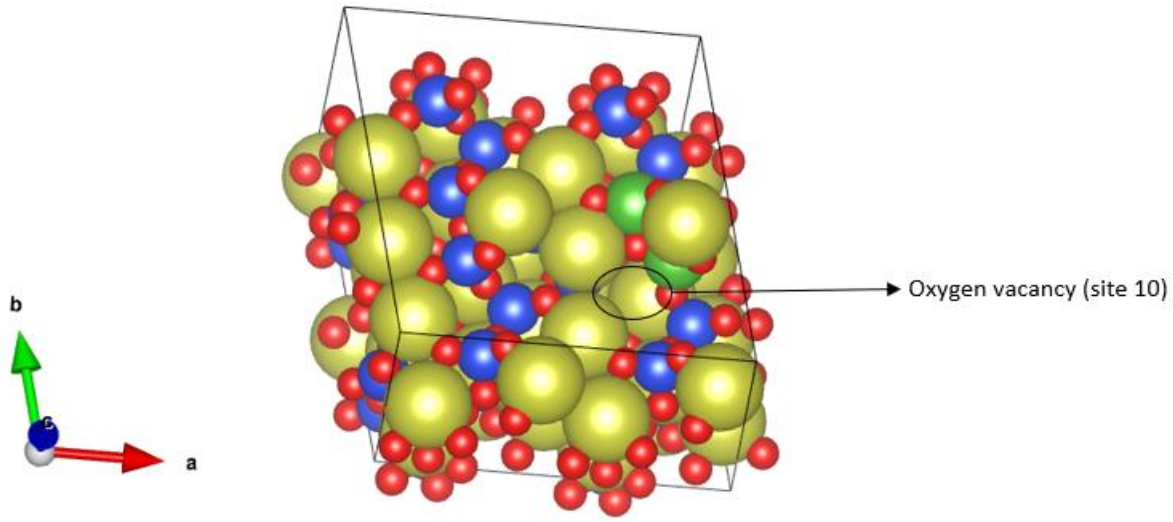

Figure 24*. Top view of the (001) surface after the formation of oxygen vacancy at site 10.*

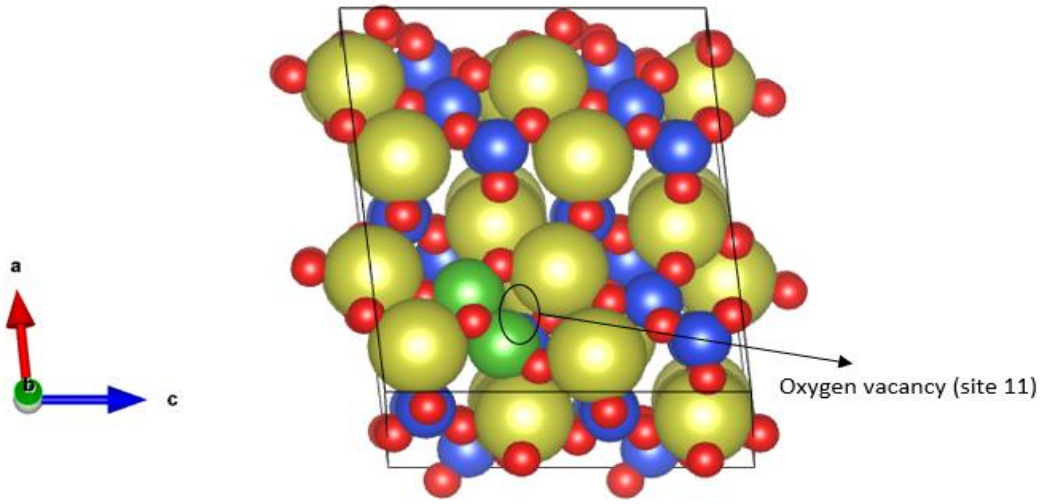

Figure 25*. Top view of the (010) surface after the formation of oxygen vacancy at site 11.*

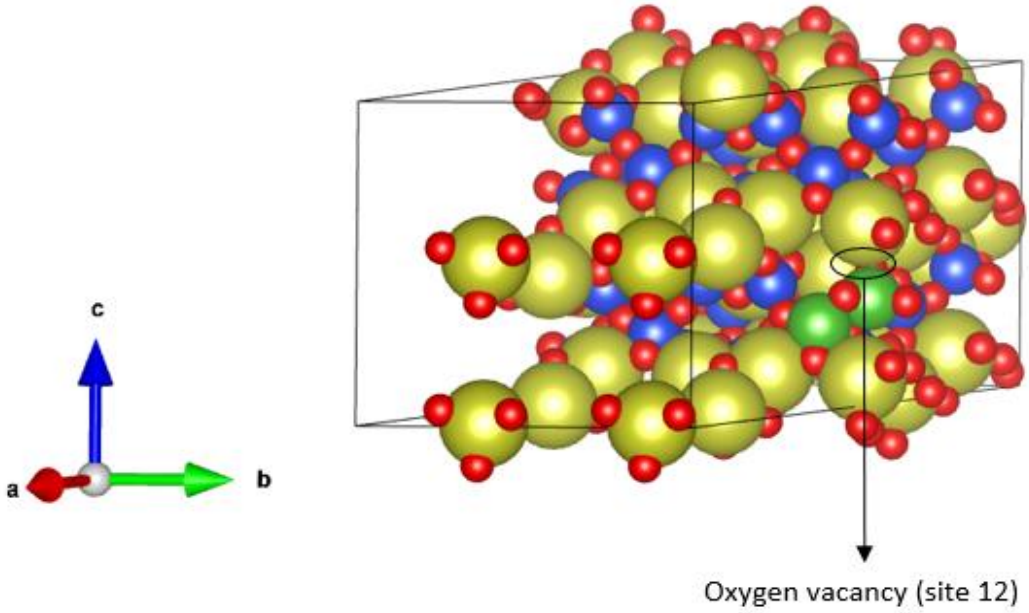

Figure 26*. Top view of the (100) surface after the formation of oxygen vacancy at site 12.*

***Table 8**. Using the total energies values from Table 8, oxygen vacancy formation energies are calculated for the aluminum doped wollastonite with the doping locations at (1NN, 2NN) with respect to the oxygen vacancy site.*

Surface	Site number	$E_{(f\ vac)}$ in eV
001	10	-0.19
010	11	0.42
100	12	-0.17

***Table 9.** Compilation of all the oxygen vacancy formation energies for aluminum doped wollastonite at different surfaces and different positions of the oxygen vacancy and dopant sites.*

Surface	Site number	Dopant atoms' locations	$E_{(f\ vac)}$ in eV
001	7	(1NN,1NN)	0.62
001	7a	(1NN,1NN)	0.57
001	10	(1NN,2NN)	-0.19
010	8	(1NN,1NN)	-0.73
010	8a	(1NN,1NN)	-0.73
010	11	(1NN,2NN)	0.42
100	9	(1NN,1NN)	-1.24
100	9'	(1NN,1NN)	-1.07
100	12	(1NN,2NN)	-0.17

We can see from the above table that (100) surface has the lowest oxygen vacancy formation energies compared to the surfaces (001) and (010). Also, the surface (001) is relatively the least favored for oxygen vacancy formation. Among all the oxygen vacancy formation energies computed in this work, the lowest / most stable formation of oxygen vacancy occurs in the scenario where the dopant sites are at (1NN, 1NN) locations with respect to the oxygen vacancy. This can be further explained using the **Figure 27.**

(a) (001)

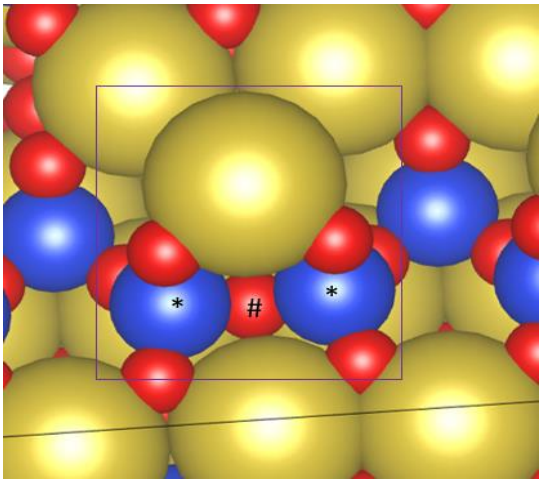

(b) (001)

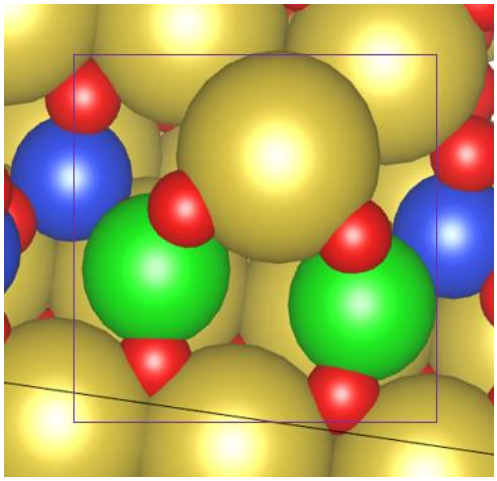

(c) (010)

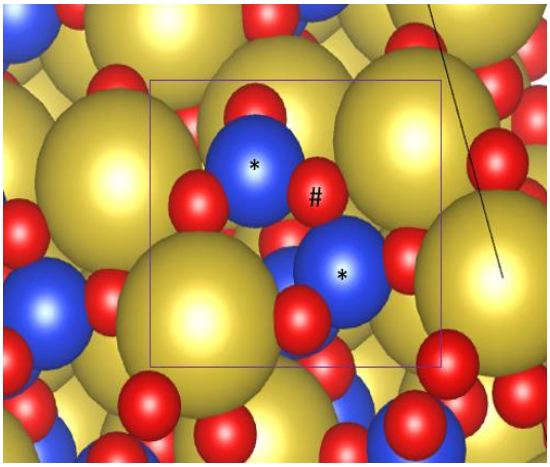

(d) (010)

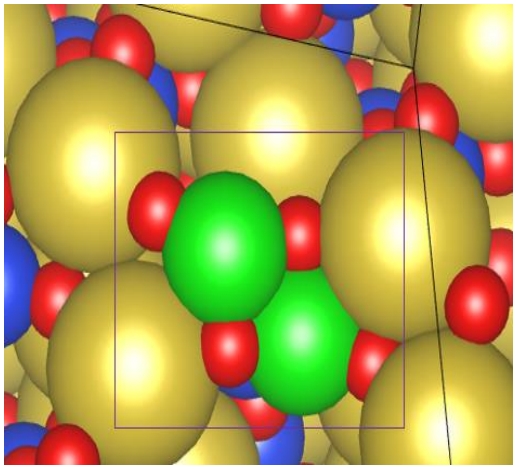

(e) (100) (f) (100)

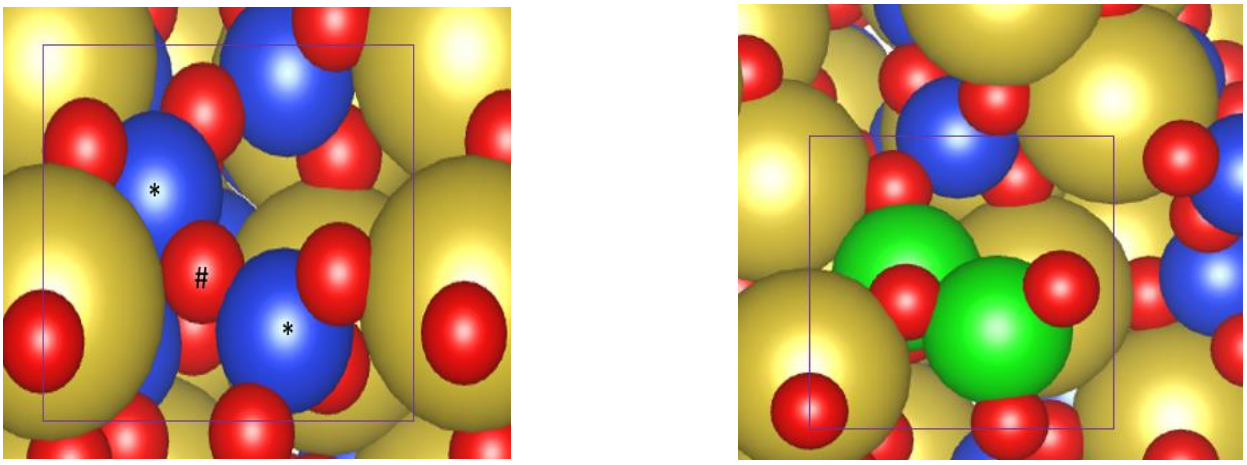

Figure 27. (a), (c) and (e) show the magnified views of the silicon atom sites and the oxygen atom site before the formation of oxygen vacancy for the surfaces (001), (010) and (100) respectively. (b), (d) and (f) show the magnified views after the formation of oxygen vacancy with the introduction of aluminum dopants for the surfaces (001), (010) and (100) respectively.

In the figures **27 (a), (c)** and **(e),** the silicon atoms marked with " * " are the ones that will be replaced with aluminum dopants and the oxygen atom marked with " # " will leave a vacancy in the crystal on addition of aluminum dopants. The silicon atoms carry +4 charge each (Si^{4+}) and they are bonded to 4 neighboring oxygen atoms. When they are replaced with two aluminum dopants carrying +3 charge each (Al^{3+}), there is a significant change in the structure as observed in the **Figures 27 (d)** and **(f)** for (010) and (100) surfaces, respectively. We can see that oxygen atoms adjacent to the aluminum dopants orient themselves in such a way that they form O-Al-O-Al-O bonds thus forming the structure of Al_2O_3 and the formation of oxygen vacancy as discussed earlier. But, for the (001) surface shown in **Figure 27 (b)**, we can find that there is no significant structural change after addition of aluminum dopants and, there are gaps present between the 2

aluminum atoms unlike what is observed for the surfaces (010) and (100), where the aluminum atoms are close to each other suggesting that they are bonded well with the neighboring atoms. This structural variation observed for the (001) surface is complementary to its positive oxygen vacancy formation energies in **Table 9**. This means that the structural change occurring for the (001) surface after adding aluminum dopants is not quite stable compared to the structural changes occurring in (010) and (100) surfaces. The negative values of oxygen vacancy formation energies for the surfaces (010) and (100) further proves the point.

4.3 Density of states analysis

By comparing density of states (DOS) before and after inclusion of oxygen vacancies and corresponding dopants, modifications in the electronic states can be visualized near the Fermi level. Detailed DOS analysis was performed to gain insights into the electronic structure of the wollastonite surface for the following scenarios: undoped wollastonite surface without oxygen vacancy; undoped wollastonite surface with oxygen vacancy; doped wollastonite surface with oxygen vacancy.

The DOS plots inform us about the band gap in a material by identifying the electronic states near the Fermi level. By comparing the DOS plots before and after a change to the system, paying close attention to the states near the Fermi level, we can see how electron states have changed and more importantly if the band gap is increasing or decreasing. This is important here because we get to know if there is any major change in the electronic structure of the wollastonite crystal when aluminum dopants are introduced.

For this purpose, we have studied the DOS plots for lowest values of oxygen vacancy formation energies for all the 3 surfaces ((001), (010) and (100)) and for all the three cases mentioned above. However, we have considered the DOS plots of only the (001) surface for our discussion.

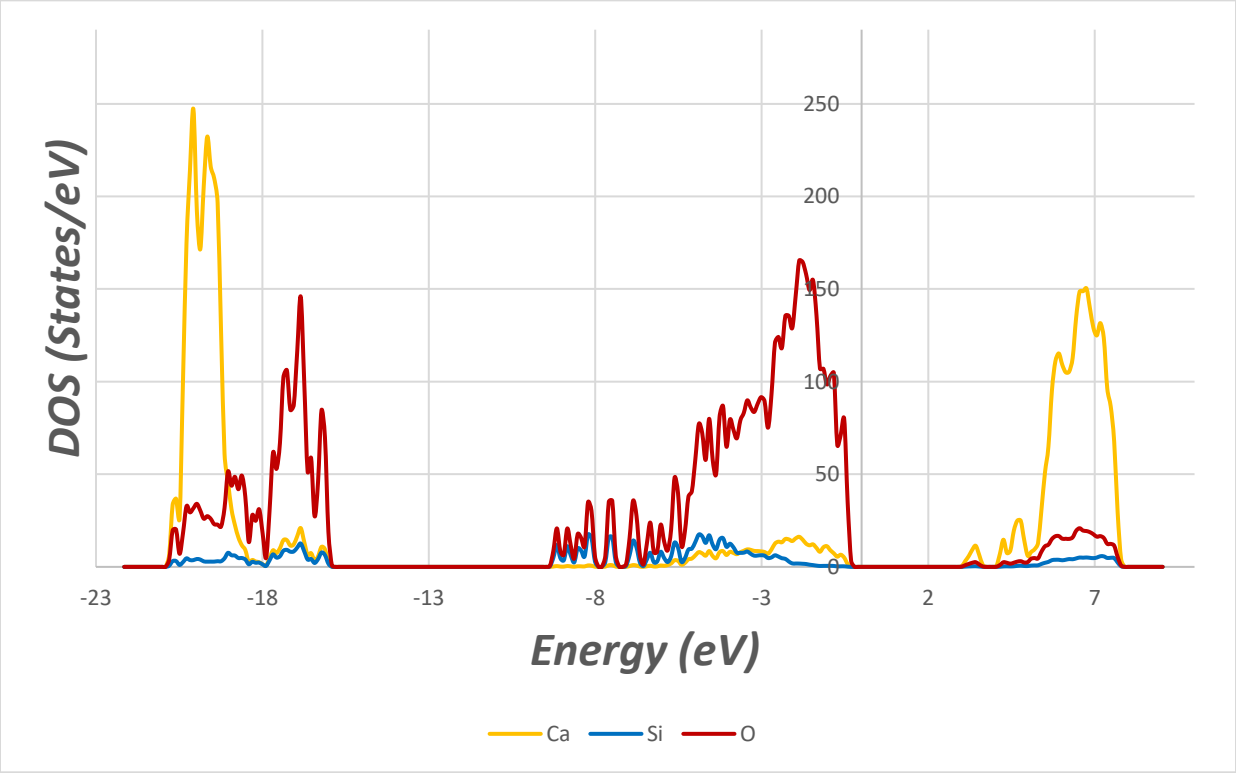

Figure 28*. Electronic density of states (DOS) projected onto Ca, Si and O atoms of the undoped defect-free (001) wollastonite surface. The Fermi energy level is shifted to 0 eV.*

From the DOS plot in Figure 27, we can observe that at the lower energy valence bands (between -13 eV and -23 eV), calcium atoms occupy many electron states with a peak of 250 states per eV. Oxygen atoms have the second highest number of energy states with a peak of 100 states

per eV, followed by silicon atoms that occupy very low number of states. At higher energy valence bands (between -9 eV and 0 eV) less than the Fermi level, oxygen atoms tend to occupy more energy states whereas calcium and silicon occupy a smaller number of energy states. Above the Fermi level of 0 eV, calcium atoms occupy relatively a very high number of energy states in the conduction bands compared to oxygen and silicon atoms.

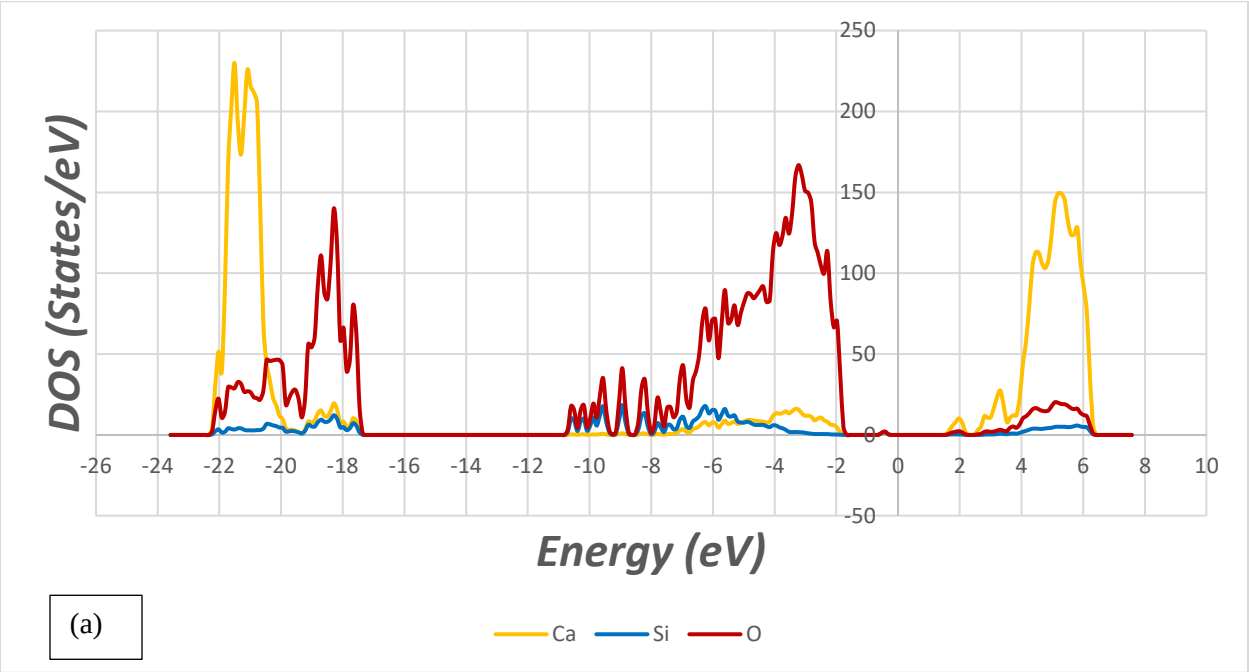

(a)

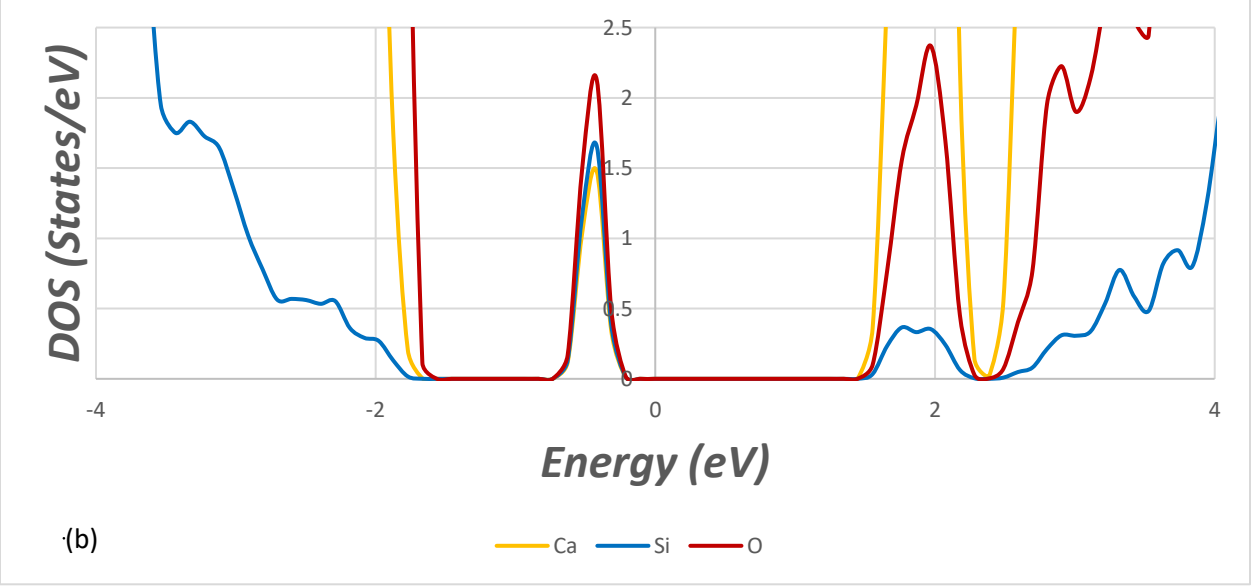

(b)

Figure 29*. (a) Electronic density of states (DOS) projected onto Ca, Si and O atoms of the (001) wollastonite surface without doping but with an oxygen vacancy. The Fermi energy level is shifted to 0 eV. (b) Magnified region near the Fermi level is shown.*

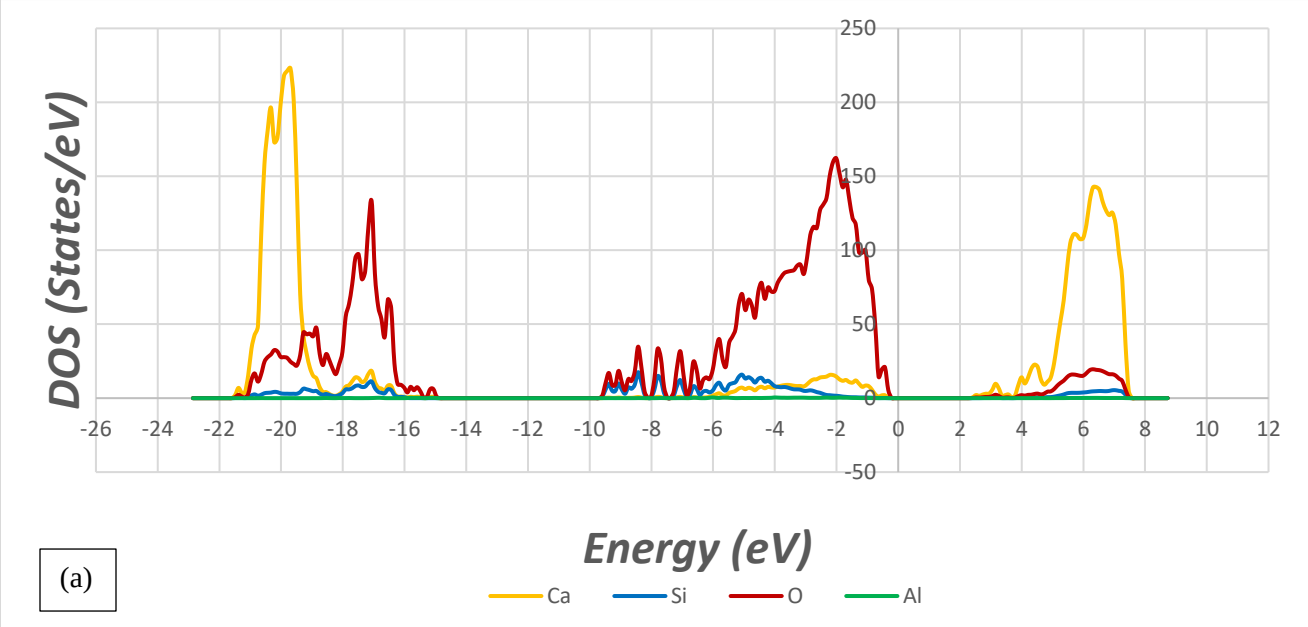

(a)

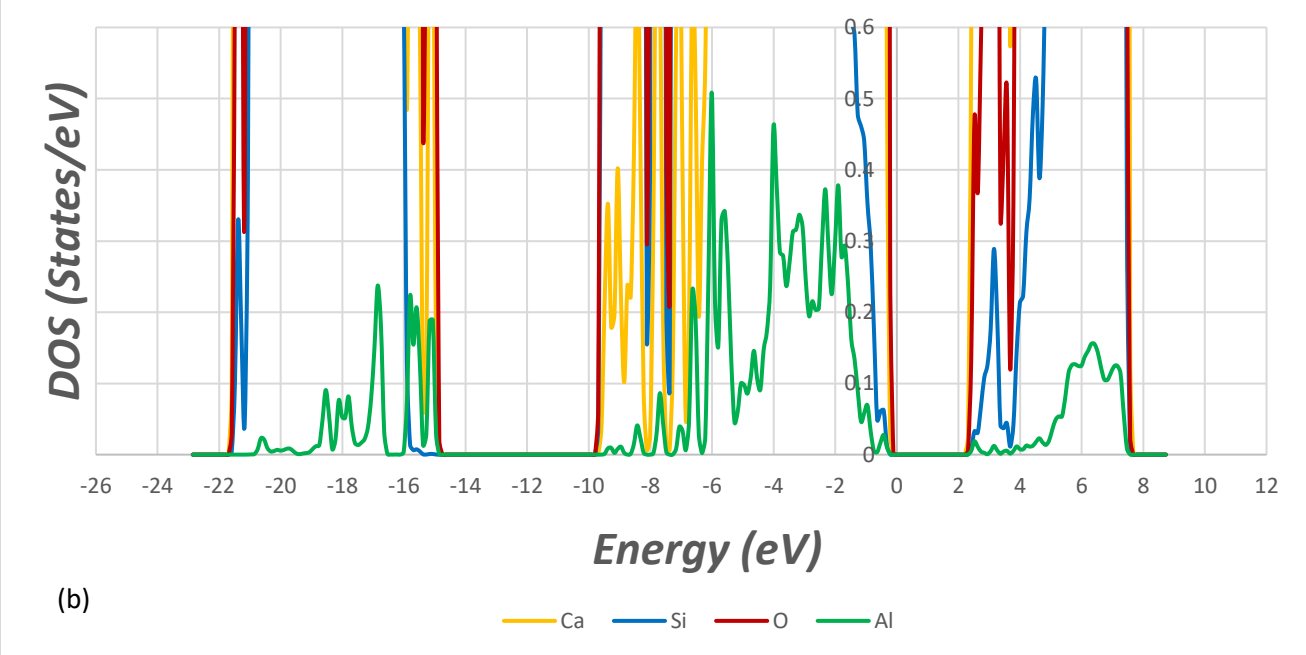

(b)

Figure 30*. (a) Electronic density of states (DOS) projected onto Ca, Si and O atoms of the aluminum doped (001) wollastonite surface with an oxygen vacancy. The Fermi energy level is shifted to 0 eV. (b) Magnified region for aluminum energy states is shown.*

With the introduction of an oxygen vacancy in the 001 surface, we can observe in **Figure 28b** that a new peak predominantly comprising of oxygen atom states arises between the top of the valence band and the bottom of the conduction band whereas the Fermi level is now positioned in the gap between this new peak and the unoccupied calcium atom states. Emergence of this new peak in the gap is often known as the metal-induced gap state (MIGS)[38]. When the oxygen vacancy is introduced, it results in two excess electrons. These excess electrons localize with the adjacent atomic orbitals resulting in the reduction of silicon atoms and gives rise to the gap states. Except for the new peak in the gap states, the compositions of valence and conduction bands are more or less similar to those observed in the undoped defect-free (001) wollastonite surface (**Figure 27**). The DOS plot for a doped (001) wollastonite surface with an oxygen vacancy (**Figure 29a**) show all the peaks in the higher energy valence bands slightly shifted closer to the Fermi level. We can visibly see (the peaks have shifted by approximately 1 eV towards the right) that a greater number of oxygen atoms occupy the higher energy valence band states compared to those in the case of an undoped defect-free (001) wollastonite surface (**Figure 27**). Also, due to the presence of aluminum dopants the gap states have disappeared as shown in **Figure 29a.** The aluminum atoms occupy relatively a much lower number of high energy valence band states compared to oxygen atoms and even compared to silicon and calcium atoms. This might probably be due to the low number of aluminum atoms (we dope the structure with just 2 aluminum atoms) in the supercell compared to the other atoms. Also, from the **Figure 29b** we can see that the peaks belonging to the aluminum atoms coincide with the peaks belonging to calcium and silicon atoms. This tells us that the

aluminum atoms bond well with the atoms present on the (001) wollastonite surface. This further demonstrates that aluminum atoms are beneficial for doping the wollastonite surface to create oxygen vacancies. The DOS plots for the surfaces not explicitly covered in the **Results** section can be found in the **Appendix** (**Figures A.5 – A.10).**

Chapter 5 – Conclusions

The following key conclusions can be drawn from this thesis:

- Formation of oxygen vacancy on the surface of wollastonite naturally requires large amount of energy.
- Oxygen vacancy formation is more favorable on the surface of the wollastonite rather than in the bulk.
- Doping the surface of the wollastonite lead to formation of oxygen vacancies, which are exothermic in most cases.
- Doping at (100) surface and with the dopant atom sites at (1NN,1NN) locations with respect to the oxygen vacancy site is the best configuration for creating an oxygen vacancy.

We thereby conclude that the formation of oxygen vacancy can be caused by doping the surface of the wollastonite crystal with aluminum atoms. Based on previous studies by other researchers[39], we expect that the formation of oxygen vacancy using aluminum dopants can enhance the carbon dioxide sequestration process on wollastonite surfaces with the following explanation. It has been observed that the carbonation reaction progressively decreases with time and stops due to deposition of the product layers. This is where the oxygen vacancies might come into play. By doping wollastonite with Al^{3+} atoms, the diffusion can be improved in the bulk layers of the crystal due to the tunneling effect produced from the oxygen vacancies that are formed. Thus, the presence of oxygen vacancies in the wollastonite crystal could potentially assist in sequestering the atmospheric carbon dioxide more efficiently. But whether this is the only way

that the oxygen vacancies contribute to carbon dioxide sequestration is a topic for future studies involving carbon dioxide adsorption on doped wollastonite surfaces, which could provide further insights into the effectiveness of aluminum dopants.

Appendix

Figure A.1. *Top view of the (010) surface showing the oxygen atom that will be removed from wollastonite.*

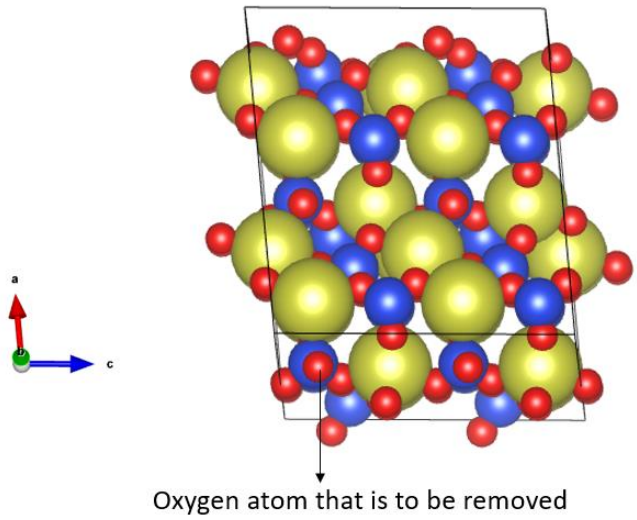

Figure A.2. *Top view of the (010) surface showing the missing oxygen atom (vacancy).*

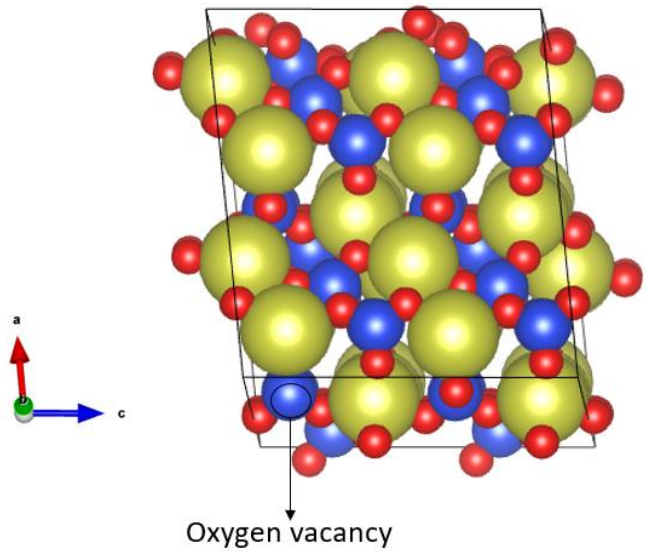

Figure A.3*. Top view of the (100) surface showing the oxygen atom that will be removed from wollastonite.*

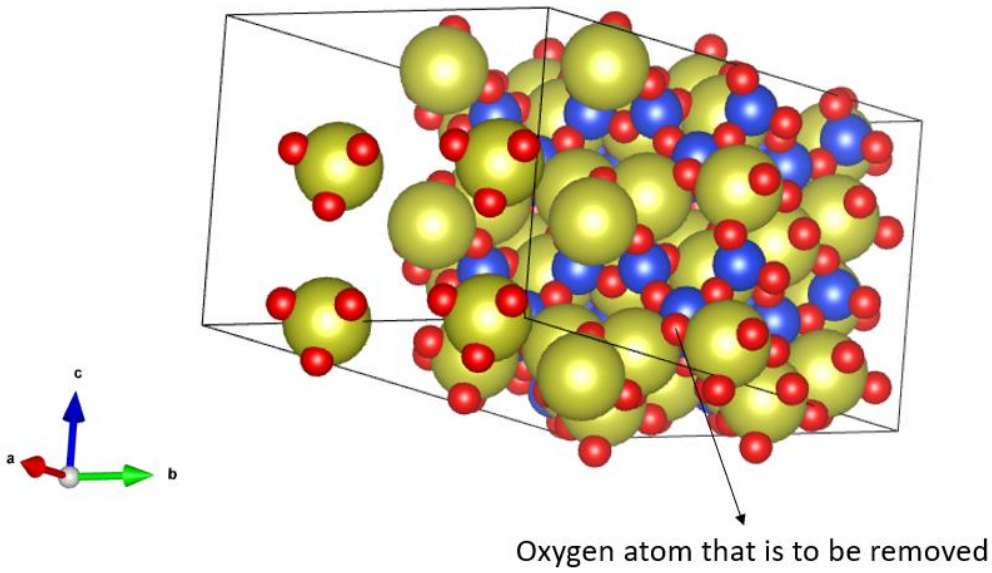

Figure A.4*. Top view of the (100) surface showing the missing oxygen atom (vacancy).*

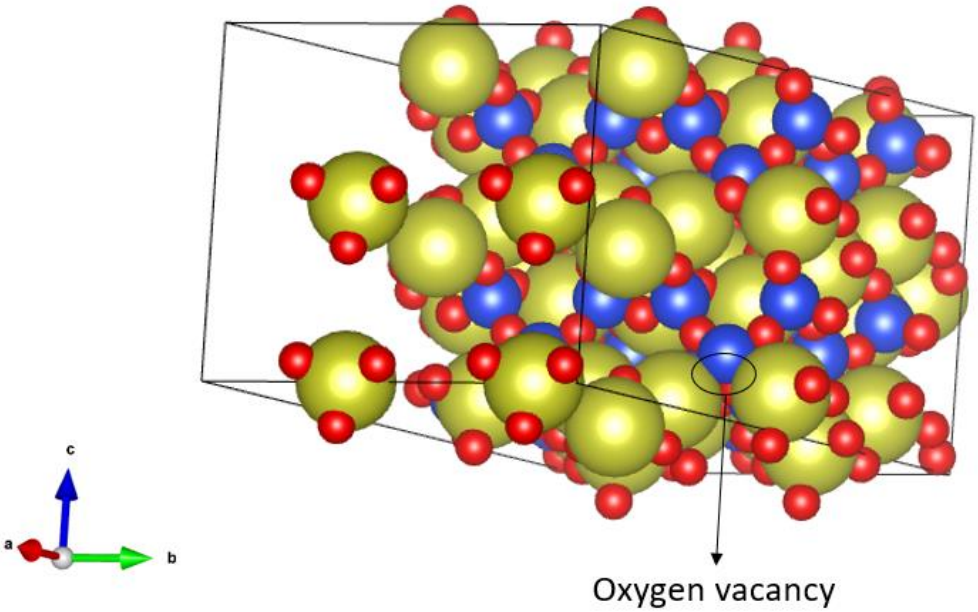

Figure A.5. *Electronic density of states (DOS) projected onto Ca, Si and O atoms for (010) wollastonite surface without doping and without oxygen vacancy. The Fermi energy level is shifted to 0 eV.*

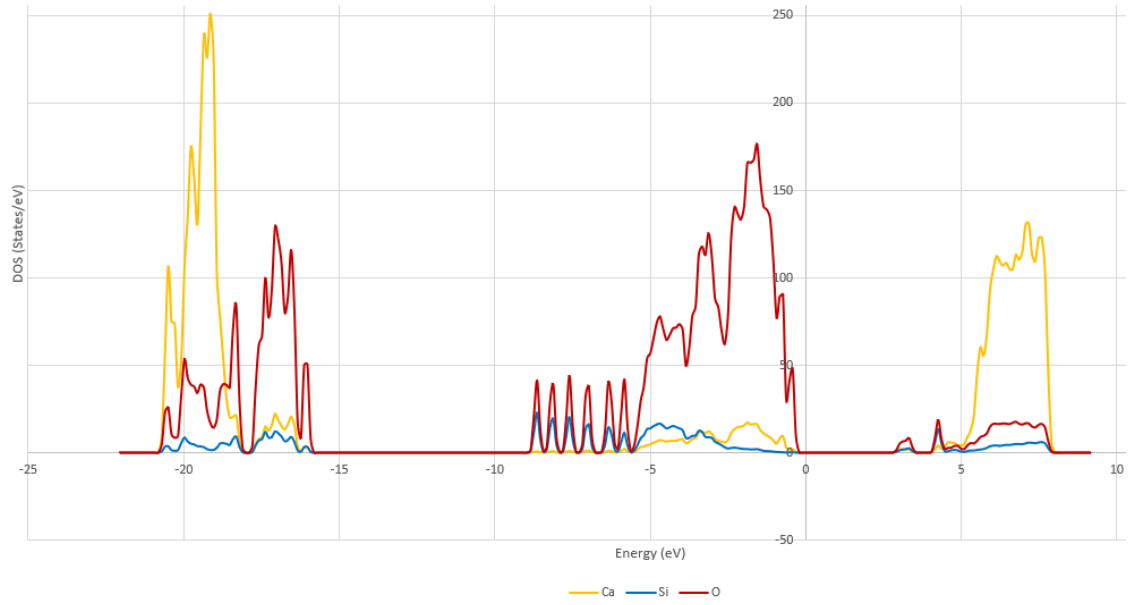

Figure A.6*. Electronic density of states (DOS) projected onto Ca, Si and O atoms for (010) wollastonite surface with oxygen vacancy but without doping. The Fermi energy level is shifted to 0 eV.*

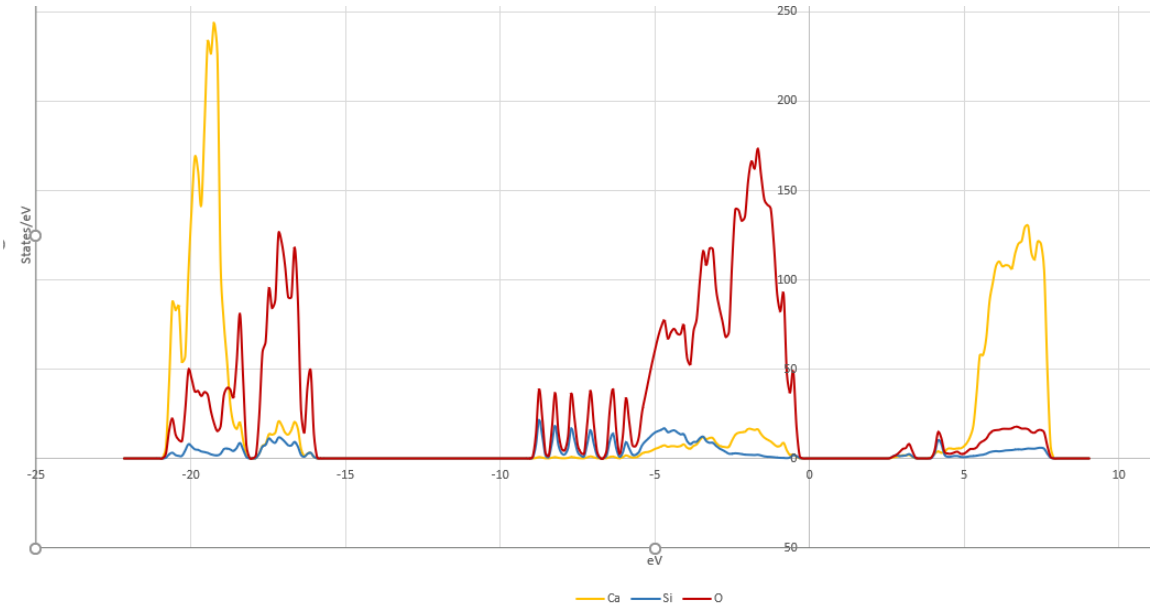

Figure A.7*. Electronic density of states (DOS) projected onto Ca, Si and O atoms for (010) wollastonite surface with oxygen vacancy and with doping. The Fermi energy level is shifted to 0 eV.*

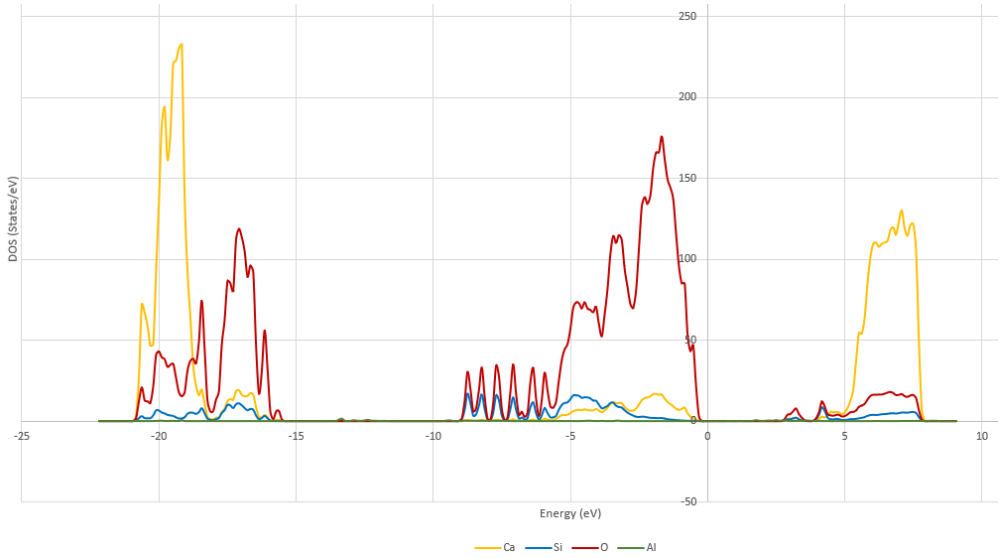

Figure A.8. *Electronic density of states (DOS) projected onto Ca, Si and O atoms for (100) wollastonite surface without doping and without oxygen vacancy. The Fermi energy level is shifted to 0 eV.*

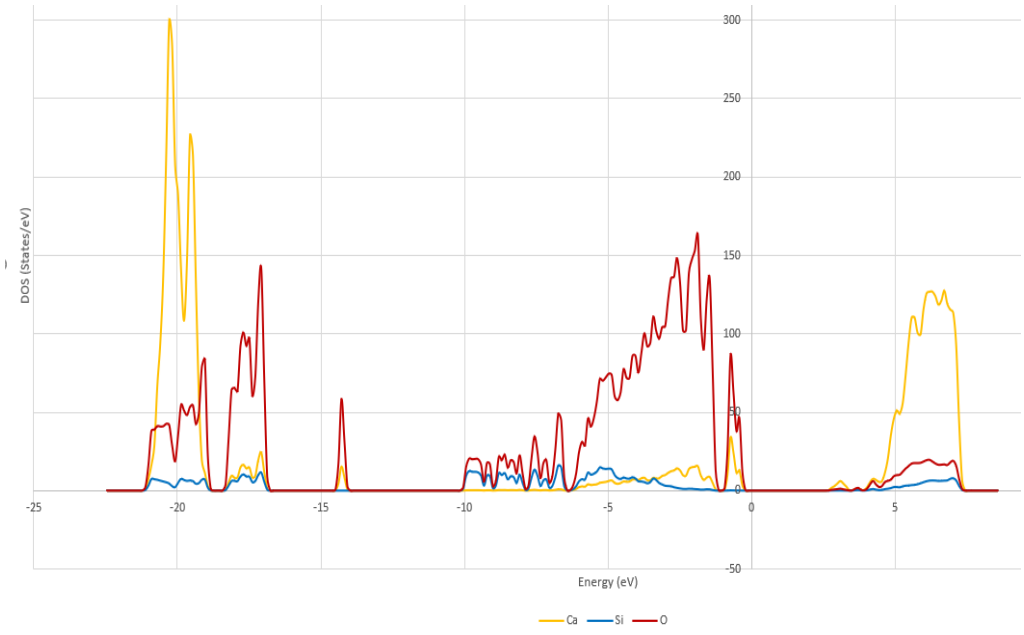

***Figure A.9**. Electronic density of states (DOS) projected onto Ca, Si and O atoms for (100) wollastonite surface with oxygen vacancy but without doping. The Fermi energy level is shifted to 0 eV.*

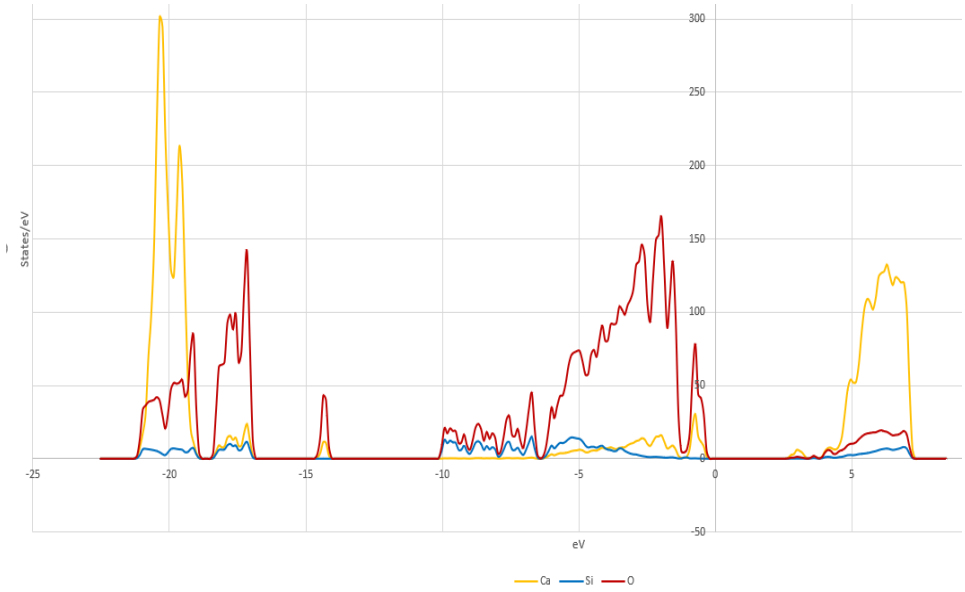

***Figure A.10**. Electronic density of states (DOS) projected onto Ca, Si and O atoms for (100) wollastonite surface with oxygen vacancy and with doping. The Fermi energy level is shifted to 0 eV.*

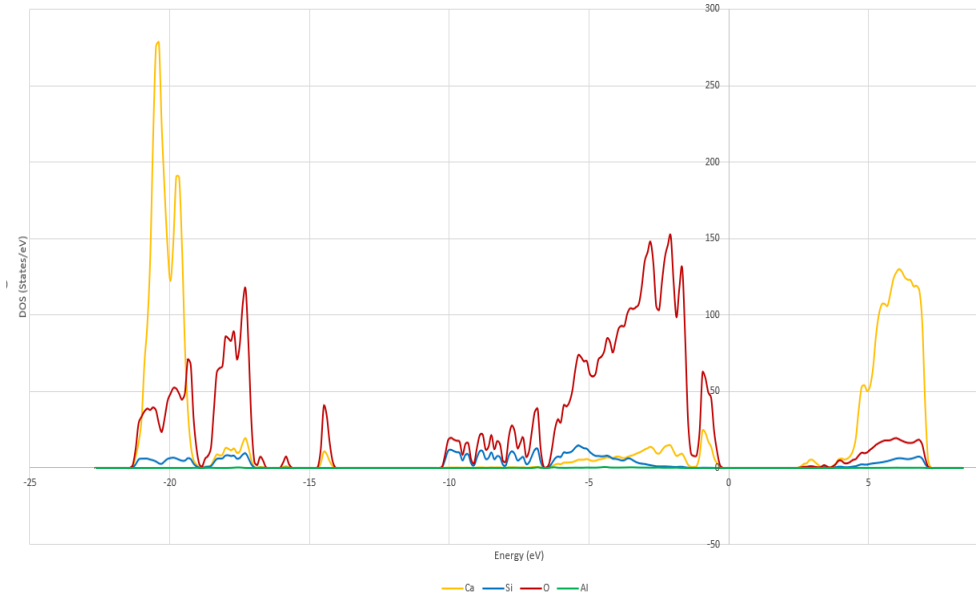

References

(1) Amanda Macmillan.; Jeff Turrentine,; *Global Warming 101*, **2021.** https://www.nrdc.org/stories/global-warming-101

(2) Noelle Eckley Selin.; *Carbon sequestration*, **2022**. https://www.britannica.com/technology/carbon-offset

(3) UC Davis,; Carbon sequestration, **2022**. https://www.ucdavis.edu/climate/definitions/carbon-sequestration

(4) Benjamin Houlton.; *Enhanced Weathering:crushed rocks spread on farmland can capture billions of tons of CO_2/year*, **2020**

(5) Burke, K. Perspective on Density Functional Theory. *J. Chem. Phys.* **2012**, *136* (15), 150901. https://doi.org/10.1063/1.4704546.

(6) Thomas, L. H. The Calculation of Atomic Fields. *Math. Proc. Camb. Philos. Soc.* **1927**, *23* (5), 542–548. https://doi.org/10.1017/S0305004100011683.

(7) Fermi, E. Statistical Method to Determine Some Properties of Atoms. *Rend Accad Naz Lincei* **1927**, *6* (602–607), 5

(8) Dirac, P. A. Note on Exchange Phenomena in the Thomas Atom. In Mathematical proceedings of the Cambridge philosophical society; Cambridge University Press, **1930**; Vol. 26, pp 376–385.

(9) Hohenberg, P.; Kohn, W. Inhomogeneous Electron Gas. *Phys. Rev.* **1964**, *136* (3B), B864–B871. https://doi.org/10.1103/PhysRev.136.B864.

(10) David S Sholl.; Janice A Steckel.; *Density Functional Theory: A practical introduction*, **2009.**

(11) P Hohenberg.; W Kohn.; Inhomogenous Electron Gas, 1964.

(12) Kohn, W.; Sham, L.J.; *Self-Consistent Equations Including Exchange and Correlation effects*, **1965,** *140* (4A), A1133–A1138. https://link.aps.org/ doi/10.1103/PhysRev.140.A1133

(13) Hohenberg, P.; Kohn, W. Inhomogeneous Electron Gas. *Phys. Rev.* **1964**, *136* (3B), B864–B871. https://doi.org/10.1103/PhysRev.136.B864

(14) Sumudu Nimasha.; Sashikesh Ganeshalingam.; Navaratnarajah Kuganathan.; Konstantinos Davazoglou.; Alexander Chroneos. Defects and Calcium Diffusion in Wollastonite, **2020**, 2, 937-946, doi:10.3390/chemistry2040059

(15) Ohashi, Y. Polysynthetically-Twinned Structures of Enstatite and Wollastonite. Phys. Chem. Miner. 1984, 10 (5), 217–229. https://doi.org/10.1007/BF00309314.

(16) Mamedov, Kh. S.; Belov, N. V. The Crystal Structure of Wollastonite. *Dokl. Akad. Nauk SSSR* **1956**, *107*, 463–466.

(17) Buerger, M. J.; Prewitt, C. T. The Crystal Structures of Wollastonite and Pectolite. *Proc. Natl. Acad. Sci. USA* **1961**, *47*, 1884–1888.

(18) Ito, T.; Sadanaga, R.; Takeuchi, Y.; Tokonami, M. The Existence of Partial Mirrors in Wollastonite. *Proc. Jpn. Acad.* **1969**, *45*, 913–918.

(19) Milani, S.; Comboni, D.; Lotti, P.; Fumagalli, P.; Ziberna, L.; Maurice, J.; Hanfland, M.; Merlini, M. Crystal Structure Evolution of CaSiO3 Polymorphs at Earth's Mantle Pressures. *Minerals* **2021**, *11* (6), 652. https://doi.org/10.3390/min11060652.

(20) Kerisit, S.; Bylaska, E. J.; Felmy, A. R. Water and Carbon Dioxide Adsorption at Olivine Surfaces. *Chem. Geol.* **2013**, *359*, 81–89. https://doi.org/10.1016/j.chemgeo.2013.10.004.

(21) Longo, R. C.; Cho, K.; Brüner, P.; Welle, A.; Gerdes, A.; Thissen, P. Carbonation of Wollastonite(001) Competing Hydration: Microscopic Insights from Ion Spectroscopy and Density Functional Theory. *ACS Appl. Mater. Interfaces* **2015**, *7* (8), 4706–4712. https://doi.org/10.1021/am508313g.

(22) Kundu, T. K.; Hanumantha Rao, K.; Parker, S. C. Atomistic Simulation of the Surface Structure of Wollastonite and Adsorption Phenomena Relevant to Flotation. *Int. J. Miner. Process.* **2003**, *72* (1–4), 111–127.

(23) Kundu, T. K.; Hanumantha Rao, K.; Parker, S. C. Atomistic Simulation of the Surface Structure of Wollastonite. *Chem. Phys. Lett.* **2003**, *377* (1–2), 81–92. https://doi.org/10.1016/S0009-2614(03)01097-2.

(24) Prigiobbe, V.; Suarez Negreira, A.; Wilcox, J. Interaction between Olivine and Water Based on Density Functional Theory Calculations. *J. Phys. Chem. C* **2013**, *117* (41), 21203–21216.

(25) Momma, K.; Izumi, F. *VESTA 3* for Three-Dimensional Visualization of Crystal, Volumetric and Morphology Data. *J. Appl. Crystallogr.* **2011**, *44* (6), 1272–1276. https://doi.org/10.1107/S0021889811038970.

(26) Momma, K.; Izumi, F. *VESTA* : A Three-Dimensional Visualization System for Electronic and Structural Analysis. *J. Appl. Crystallogr.* **2008**, *41* (3), 653–658. https://doi.org/10.1107/S0021889808012016.

(27) Kresse, G.; Hafner, J. Ab Initio Molecular Dynamics for Liquid Metals. *Phys. Rev. B* **1993**, *47* (1), 558–561.

(28) Kresse, G.; Hafner, J. Ab Initio Molecular-Dynamics Simulation of the Liquid-Metal--Amorphous-Semiconductor Transition in Germanium. *Phys. Rev. B* **1994**, *49* (20), 14251–14269.

(29) Kresse, G.; Furthmüller, J. Efficiency of Ab-Initio Total Energy Calculations for Metals and Semiconductors Using a Plane-Wave Basis Set. *Comput. Mater. Sci.* **1996**, *6* (1), 15–50.

(30) Kresse, G.; Furthmüller, J. Efficient Iterative Schemes for Ab Initio Total-Energy Calculations Using a Plane-Wave Basis Set. *Phys. Rev. B* **1996**, *54* (16), 11169– 11186.

(31) Hafner, J. Ab-Initio Simulations of Materials Using VASP: Density-Functional Theory and Beyond. *J. Comput. Chem.* **2008**, *29* (13), 2044–2078. https://doi.org/10.1002/jcc.21057.

(32) Kresse, G. VASP the Guide. *Httpcms Mpi Univie Ac Atvasp* **2001**.

(33) Sanna, S.; Schmidt, W. G.; Thissen, P. Formation of Hydroxyl Groups at Calcium- Silicate-Hydrate (C-S-H): Coexistence of Ca–OH and Si–OH on Wollastonite(001). *J. Phys. Chem. C* **2014**, *118* (15), 8007–8013. https://doi.org/10.1021/jp500170t.

(34) Perdew, J. P.; Burke, K.; Ernzerhof, M. Generalized Gradient Approximation Made Simple. *Phys. Rev. Lett.* **1996**, *77* (18), 3865–3868. https://doi.org/10.1103/PhysRevLett.77.3865.

(35) Ernzerhof, M.; Perdew, J. P. Generalized Gradient Approximation to the Angle- and System-Averaged Exchange Hole. *J. Chem. Phys.* **1998**, *109* (9), 3313–3320. https://doi.org/10.1063/1.476928.

(36) B Luan and P. P. Dholabhai. First Principles Modeling of CO_2 adsorption on (100), (010), and (001) Surfaces of Wollastonite for Applications in Enhanced Rock Weathering. *Surface Science.* **2022,** 724, 122143. https://doi.org/10.1016/j.susc.2022.122143

(37) Kohn, W. Nobel Lecture: Electronic Structure of Matter—Wave Functions and Density Functionals. *Rev. Mod. Phys.* **1999**, *71* (5), 1253–1266. https://doi.org/10.1103/RevModPhys.71.1253.

(38) P. P. Dholabhai. Oxygen Vacancy Formation and Interface Charge Transfer at Misfit Dislocations in Gd-Doped CeO_2/MgO Heterostructure. *Journal of Physical Chemistry C*. **2022,** 126, 11735-11750.

https://doi.org/10.1021/acs.jpcc.2c02009

(39) Yadav, S.; Mehra, A. Mathematical modelling and experimental study of carbonation of wollastonite in the aqueous media. *Journal of CO2 Utilization.* **2019,** *31, 181–191.* https://doi:10.1016/j.jcou.2019.03.013 .

(40) P.P Dholabhai.; James B. Adams. A blend of first principles and kinetic lattice Monte Carlo computation to optimize samarium-doped ceria. *J Mater Sci*. **2012**, 47:7530–7541

(41) The Materials Project Wollastonite structure https://materialsproject.org/materials/mp-5733 .